Atmos. Chem. Phys., 25, 16797–16816, 2025 https://doi.org/10.5194/acp-25-16797-2025 © Author(s) 2025. This work is distributed under the Creative Commons Attribution 4.0 License.





# HONO formation mechanisms and impacts on ambient oxidants in coastal regions of Fujian, China

Haoran Zhang<sup>1</sup>, Chengchun Shi<sup>2,3</sup>, Chuanyou Ying<sup>1,4</sup>, Shengheng Weng<sup>5</sup>, Erling Ni<sup>2,3</sup>, Lanbu Zhao<sup>1</sup>, Peiheng Yang<sup>1</sup>, Keqin Tang<sup>6</sup>, Xueyu Zhou<sup>1</sup>, Chuanhua Ren<sup>1</sup>, Xuguang Chi<sup>1</sup>, Derong Zhou<sup>7</sup>, Mengmeng Li<sup>1</sup>, Nan Li<sup>6</sup>, Tengyu Liu<sup>1</sup>, and Xin Huang<sup>1</sup>

Correspondence: Xin Huang (xinhuang@nju.edu.cn)

Received: 4 June 2025 – Discussion started: 8 August 2025 Revised: 14 October 2025 – Accepted: 27 October 2025 – Published: 25 November 2025

Abstract. Nitrous acid (HONO) is a vital precursor of hydroxyl radicals (OH) in the troposphere, leading to the formation of secondary air pollutants, including ozone (O<sub>3</sub>) and secondary aerosols. Previous studies have mainly focused on investigating the chemical fate of HONO in polluted urban areas of China and found a general diurnal variation featuring the minimum concentration around noon due to the fast self-photodissociation. However, this study reported a significantly higher daytime HONO concentrations based on one-month measurement during May 2024 over the coastal regions of Fujian in southeastern China. Using an updated Weather Research and Forecasting coupled with Chemistry (WRF-Chem) model, we captured the magnitude and temporal variation of HONO concentrations observed in coastal areas, and improved the model performance on diurnal patterns of the NO<sub>2</sub> and O<sub>3</sub>. Further process analysis revealed that two light-dependent chemical sources, i.e., the heterogeneous uptake of  $NO_2$  on the ground surface and  $NO_x$  photo-oxidation, were the main contributors to HONO formation, particularly at high concentrations around noon in the presence of persistent intensive solar radiation. In addition, we assessed that shipping emissions contributed 20 % to the midday HONO production rate in coastal regions. Subsequently, model results indicated that HONO photolysis accounted for 34 % of primary OH sources during the daytime. Model sensitivity experiments demonstrated that incorporating multiple HONO sources increased the daily maximum OH and average O<sub>3</sub> concentrations by 61 % and 44 %, respectively, in coastal regions. Overall, this study highlights the unique formation mechanisms of HONO and its significant contribution to ambient oxidants in typical coastal regions.

# 1 Introduction

Nitrous acid (HONO) is an unstable reactive nitrogen species. It can be generated through various formation pathways, such as direct emissions from combustion-related processes, soils, and fertilization (Kurtenbach et al., 2001; Oswald et al., 2013; Ren et al., 2025; Su et al., 2011; Tan et al., 2023), the homogeneous reaction between NO and OH (Reaction R1) (Sarwar et al., 2008), light-enhanced NO<sub>2</sub> heterogeneous uptake on solid surfaces (Reaction R2) (Finlayson-Pitts et al., 2003; George et al., 2015; Kim et al., 2024), and photolysis of particulate nitrate aerosols (Reaction R3) (Ye et al., 2016, 2017). In addition, a recent laboratory study also reported that the photo- and dark-oxidation of nitrogen oxides (NO<sub>x</sub>) could significantly contribute to HONO formation (Reactions R4 and R5) (Song et al., 2023).

$$NO + OH \rightarrow HONO$$
 (R1)

$$2NO_2 + H_2O + h\nu \xrightarrow{\text{surface}} HONO + HNO_3$$
 (R2)

$$pNO_3^- + h\nu \to 0.67HONO + 0.33NO_2$$
 (R3)

$$HNO_3 + NO \rightarrow HONO + NO_2$$
 (R4)

$$NO_3 + NO \rightarrow 1.98NO_2 + 0.02HONO$$
 (R5)

In the presence of sunlight, HONO can rapidly undergo photodissociation (Reaction R6) to yield NO and OH radicals (Seinfeld and Pandis, 2016). Meanwhile, HONO can be slightly consumed by OH oxidation (Reaction R7). The photolytic process of HONO plays a vital role in maintaining the atmospheric oxidizing capacity (AOC) and facilitating the formation of secondary air pollutants (Kleffmann et al., 2005). For example, during the daytime, the oxidation of NO<sub>2</sub> by OH usually results in the production of nitric acid (HNO<sub>3</sub>) (Reaction R8), which subsequently reacts with ammonia (NH<sub>3</sub>) to form inorganic nitrate aerosols (Reaction R9). Additionally, OH radicals can degrade volatile organic compounds (VOCs), leading to the formation of RO2 radicals (Reaction R10) that further contribute to the generation of secondary organic aerosols (SOA) (Wang et al., 2017). Concurrently, RO<sub>2</sub> can react with NO to produce NO<sub>2</sub> (Reaction R11), a reaction that reduces ozone (O<sub>3</sub>) titration (Reaction R12) while providing NO<sub>2</sub> for the subsequent formation of O<sub>3</sub> through Reactions (R13) and (R14). The associated reactive rate constants of these listed gaseous and photolysis reactions are well documented in Carter (2000).

$$HONO \rightarrow OH + NO$$
 (R6)

$$HONO + OH \rightarrow NO_2 + H_2O \tag{R7}$$

$$OH + NO_2 \rightarrow HNO_3$$
 (R8)

$$HNO_3 + NH_3 \rightarrow NH_4NO_3$$
 (R9)

$$VOC + OH \rightarrow RO_2 + H_2O \tag{R10}$$

$$RO_2 + NO \rightarrow RO + NO_2 \tag{R11}$$

$$O_3 + NO \rightarrow O_2 + NO_2 \tag{R12}$$

$$NO_2 + h\nu \to O^3 P + NO \tag{R13}$$

$$O^3 P + O_2 \to O_3 \tag{R14}$$

Over the past decade, there has been a notable increase in research interests about the topics related to HONO due to its critical potential to induce secondary air pollution in China (Jiang et al., 2024; Xue, 2022). The majority of previous studies have focused on elucidating the mechanisms of HONO formation and its associated environmental impacts, especially in city clusters of China that frequently experience severe air pollution (Fu et al., 2019; Li et al., 2022; Ran et al., 2024; Zhang et al., 2021, 2022c, 2023). For instance, Fu et al. (2019) demonstrated that HONO can intensify O<sub>3</sub> pollution by up to 24 ppbv during haze events in the Pearl River Delta (PRD) region of China. Meanwhile, Zhang et al. (2021) concluded that the enhanced AOC conditions contributed by HONO chemistry increased secondary aerosol concentrations by 18 %-51 % in the North China Plain (NCP). Our previous study focused on the Yangtze River Delta (YRD) region indicates that HONO contributed to a 22 % and 28 % increase in concentrations of fine particulate matter and O<sub>3</sub> during a short-term compound air pollution case in March 2019 (Zhang et al., 2024b).

Observational studies conducted in polluted urban areas of China indicated that lower concentrations of HONO typically occurred around noon (Fu et al., 2019; Song et al., 2023; Wang et al., 2025; Zhang et al., 2021). The similar diurnal pattern of HONO concentrations was also reported by measurements in urban areas of Italy, South Korea, Japan, and the United States (Acker et al., 2006; Kim et al., 2024; Nakashima et al., 2017; Stutz et al., 2010). These lower HONO concentrations could be attributed to the fast photo-dissociation at noon. However, several in-situ observations in typical coastal regions such as Cyprus and Cape Verde revealed an inverse diurnal variation of HONO with higher concentrations occurring at noon (Crilley et al., 2021; Jiang et al., 2023; Meusel et al., 2016). In China, Zhong et al. (2023) reported that their measurement campaign in Qingdao, a coastal city adjacent to the Yellow Sea, identified an unexpected diurnal peak in HONO concentrations at 12:00 LT (local time) (UTC+8). Using the observation-based model (OBM), their study suggested that the higher HONO concentrations at noon was likely attributed to an unidentified marine source. This suggests that oceanic contributions may affect the diurnal formation of HONO on land. But the mechanisms of HONO formation in coastal regions are not well understood by existing studies. Moreover, the maritime industry is an essential source of oceanic emissions. A previous study confirmed that shipping activities can emit substantial amounts of  $NO_x$  (Liu et al., 2016). As  $NO_x$  is a key precursor of HONO, shipping emissions can considerably impact the subsequent chemical production of HONO on land near the ocean (Dai and Wang, 2021). Furthermore, HONO emissions have been acknowledged as a result of shipping activities (Ke et al., 2025; Sun et al., 2020). Sun et al. (2020) estimated that the ratio of HONO to  $NO_x$  emissions was 0.51 % based on specific measurements for ship plumes. Nevertheless, the contribution of shipping emissions to HONO formation in coastal areas has yet to be quantitatively assessed.

This study aims to investigate the mechanisms of HONO formation and its impact on the enhancement of OH radicals and O<sub>3</sub> in Fujian, a representative coastal region in southeastern China. To this end, we first conducted a one-month field measurement to characterize the levels and diurnal patterns of coastal HONO concentrations (see Sect. 3.1). We then employed the Weather Research and Forecasting model coupled with Chemistry (WRF-Chem) to reproduce the observed variations in HONO and performed a chemical budget analysis of HONO using process analysis techniques (refer to Sect. 3.2 and 3.3). The model utilized in this study is based on our previous updates of the multiple HONO sources (Zhang et al., 2024b). In Sect. 3.3, we conducted a sensitivity experiment by zeroing out shipping emissions to clarify the influence of maritime activities on coastal HONO formation. Subsequently, we assessed the contribution of HONO photolysis to elevated coastal OH radicals and O<sub>3</sub> concentrations, as described in Sect. 3.4. The relevant uncertainties in the model were discussed in Sect. 3.5. Overall, this study comprehensively integrated field measurements and threedimensional (3D) numerical simulations to improve our understanding of HONO formation mechanisms and its environmental implications for ambient oxidants in coastal regions of southeastern China.

## 2 Data and methods

#### 2.1 Field measurements and instrument

The in-situ measurement was conducted during the period from 1 to 31 May 2024. The sampling location was the Dongzhen Reservoir (DZSK, 118.98°E, 25.48°N), which was categorized as a suburban site in Putian. The DZSK site was 6 km from downtown of Putian and approximately 25 km from the Taiwan Strait. The geographical location of DZSK is shown in Fig. 1. Hourly HONO concentrations were measured using a long-path absorption photometer (LOPAP). The other two gaseous air pollutants, NO<sub>2</sub> and O<sub>3</sub>, were measured using a commercial chemiluminescence instrument (Thermo Fisher Scientific 17i and 49i). For mode 17i, we acknowledge that the chemiluminescence instrument with a molybdenum converter used for NO2 measurements may be subject to positive artifacts from other reactive nitrogen species, which represents a potential source of uncertainty in the NO<sub>2</sub> data used for model evaluation (Dunlea et al., 2007). Air temperature and relative humidity were monitored by a micro automatic weather station (LUFFT). Ultraviolet radiation (UV-A) was simultaneously observed with a solar radiation instrument (Kipp & Zonen). As records of the hourly wind field and precipitation were missing for the study period, observations were obtained from alternative sources. For wind speed and direction, we collected the  $U_{10}$  and  $V_{10}$  variables, representing wind components at 10 m, from the ERA5 reanalysis dataset archived on the European Centre for Medium-Range Weather Forecasts (ECMWF) platform. Additionally, we obtained the precipitation data observed by the regional meteorological station in Putian (119.00° E, 25.44° N) for further analysis.

# 2.2 Regional chemical transport model

WRF-Chem is one of the most widely used regional chemical transport models in atmospheric chemistry modeling (Zhang et al., 2024a). It can simulate the evolution of ambient trace gases and aerosols with fully coupled meteorologychemistry feedback (Grell et al., 2005). This study used WRF-Chem (version 4.1.5) to explore coastal HONO formation and the associated environmental influences. To align with the measurement campaign, the model was run from 26 April to 31 May 2024. The first five days were reserved for spin-up and were excluded from the data analysis. The entire WRF-Chem simulation was manually restarted every seven days to reduce the influence of the accumulation of biases from the numerical computation. The modeling domain focused on the southeastern coastal region of China (Fig. 1), with a grid spacing of 10 km. Fujian Province is highlighted in a blue dashed box in Fig. 1a. The coastal regions of Fujian consist of plains with a terrain elevation of less than 500 m. Central Fujian is occupied by longitudinal mountains. This study focuses on six coastal cities for further discussion. As shown in Fig. 1b, these cities are, from north to south: Ningde (ND), Fuzhou (FZ), Putian (PT), Quanzhou (QZ), Xiamen (XM), and Zhangzhou (ZZ). The observational site DZSK is located in the suburbs of Putian. In addition, 30 vertical layers were set up, extending from the ground surface to a height of 50 hPa.

The initial and lateral meteorological input conditions were derived from the final (FNL) global reanalysis dataset of the National Oceanic and Atmospheric Administration (NOAA). We also utilized four-dimensional data assimilation (FDDA) to constrain gridded surface and upper atmospheric parameters with extra weather observational datasets. Continental anthropogenic emissions were obtained from the Multi-resolution Emission Inventory for China (MEIC version 1.4) (Li et al., 2017; Zheng et al., 2018). Shipping emissions were obtained from the Shipping Emission Inventory Model (SEIM), which was developed by Tsinghua University (Liu et al., 2016). Figure S1 in the Supplement illustrates the spatial distribution pattern of continental and oceanic shipping emissions within the modeling domain. Biogenic emissions were calculated online using the Model of Emissions of Gases and Aerosols from Nature (MEGAN, version 2.0.6) (Guenther et al., 2006). Furthermore, this study adopted various parameterizations to predict sub-grid atmospheric physical and chemical processes. The detailed information was compiled in Table 1. The Statewide Air Pollution

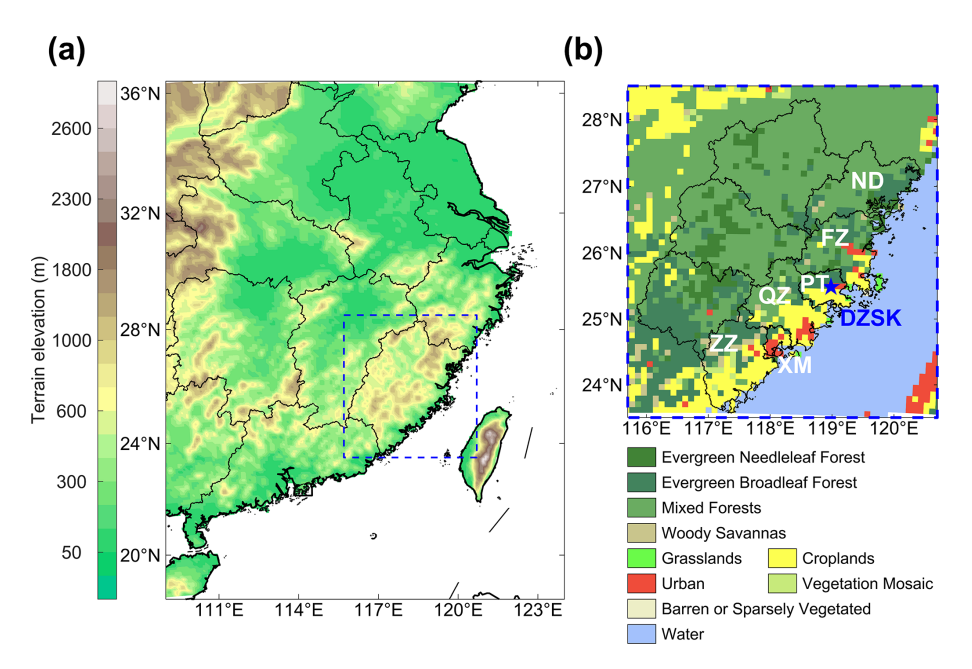


**Figure 1.** Design of the WRF-Chem modeling domain used in this study. Panel (a) depicts the terrain elevation of the modeling domain. Panel (b) illustrates the land use information in Fujian Province. The DZSK site (blue pentagram) and the six coastal cities (white bold font) are also marked in panel (b).

Research Center (SAPRC99) mechanism (Carter, 2000) and the Model for Simulating Aerosol Interactions and Chemistry (MOSAIC) (Zaveri et al., 2008) were selected for gasphase and aerosol chemistry simulations, respectively. The Fast-J module was chosen to calculate the photolytic rates of trace gases (Wild et al., 2000).

# 2.3 HONO source updates and process analyses

In the original WRF-Chem model, the default source of HONO formation is the homogeneous reaction between NO and OH radicals. In a previous study, we incorporated multiple additional HONO sources into the WRF-Chem model (Zhang et al., 2024b), including direct emissions from fuel combustion processes, photo- and dark-oxidation of  $NO_x$ , light-enhanced heterogeneous uptake of NO<sub>2</sub> on the ground and aerosol surfaces, and photolysis of particulate nitrate aerosols. Updates to the chemical parameterizations of the HONO sources are summarized in Table 2. The NO<sub>2</sub> heterogeneous uptake on ground and aerosol surfaces was parameterized as a light-dependent process, with uptake coefficients  $(\gamma)$  chosen in accordance with previous studies in China (Zhang et al., 2021, 2024b; Liu et al., 2019). The base nighttime uptake coefficients of NO<sub>2</sub> were set to  $8 \times 10^{-6}$  for the ground surface and  $4 \times 10^{-6}$  for aerosol surfaces. During the daytime, these values were dynamically increased with solar radiation using a linear equation, reaching their maximums of  $6 \times 10^{-5}$  and  $1 \times 10^{-3}$ , respectively (Liu et al., 2019).  $S_a/V$  and  $S_g/V$  are aerosol and ground surface area densities (m $^2$  m $^{-3}$ ), respectively.  $S_a/V$  could be calculated through the MOSAIC aerosol module, which categorized different types of aerosols into four size bins ranging from 3.9 nm to  $10 \,\mu\text{m}$ , i.e. 0.039-0.156, 0.156-0.625, 0.625-0.6252.500 and 2.500–10.000  $\mu$ m (Zaveri et al., 2008).  $S_g/V$  was derived based on the underlying surface category. In vegetation grid cells,  $S_g/V$  was estimated as the ratio of the two-fold of leaf area index (LAI, m<sup>2</sup> m<sup>-2</sup>) to the model height of the first layer (Zhang et al., 2016). For urban areas, the ground surface area density  $S_g/V$  was empirically set from 0.1 to 0.3 depending on the fraction of urban area using a linear formula (Zhang et al., 2024b). It is noted that the model only accounts for heterogeneous uptake of NO<sub>2</sub> on ground surface in the first layer, while the reaction on aerosol surfaces occurs in all model layers. In addition, two key parameters have been updated in this study to more accurately represent the HONO formation rate in typical coastal regions. The first parameter is the ratio of HONO to  $NO_x$  $(HONO / NO_x)$ , which reflects emission intensity. Here, we utilized the value of 1.45 % proposed by Hu et al. (2022) based on long-term in situ measurements in Xiamen, Fujian. This value more accurately represents direct HONO emissions from local fuel combustion. Simultaneously, we estimated HONO emissions from the shipping sector using the same ratio. Secondly, we set the photolysis frequency of nitrate aerosols  $(J_{NO_2^-})$  to 120 times that of gaseous HNO<sub>3</sub> (Fu et al., 2019; Ye et al., 2016, 2017).

We used a source-oriented method (SOM) to determine the proportion of HONO production and consumption processes contributed by each source. A detailed description of the SOM diagnostic module can be found in Zhang et

**Table 1.** List of WRF-Chem modeling configurations.

	Parameter	Configuration		
Time setup	Simulation duration Spin-up period	From 26 Apr to 31 May 2024 5 days		
Domain setup	Grid number Domain center Horizontal resolution Vertical configuration Projection	180 × 210 116.2° E, 27.8° N 10 km × 10 km 30 layers from surface to 50 hPa height Lambert conformal		
Physical parameterization	Microphysics Long-wave radiation Short-wave radiation Surface layer Land surface Boundary layer Cumulus	Lin (Lin et al., 1983) RRTMG (Iacono et al., 2008) RRTMG (Iacono et al., 2008) MM5 Monin–Obukhov (Jiménez et al., 2012) Noah (Chen and Dudhia, 2001) YSU (Hong et al., 2006) Grell 3D (Grell and Dévényi, 2002)		
Chemical parameterization	Gas-phase reactions Aerosol processes Photolysis	SAPRC99 (Carter, 2000) MOSAIC (Zaveri et al., 2008) Fast-J (Wild et al., 2000)		

Table 2. Chemical parameterizations of HONO sources in the revised WRF-Chem model.

Pathway	Parametrization	Descriptions			
Direct Emissions	$E_{\text{HONO}} = \frac{\text{HONO}}{\text{NO}_x} \times E_{\text{NO}_x}$	$E_{\rm HONO}$ and $E_{\rm NO_x}$ are emissions of HONO and NO <sub>x</sub> . HONO/NO <sub>x</sub> = 1.45 % (Hu et al., 2022)			
Heterogeneous uptake of NO <sub>2</sub> by ground surface	$k_g = \frac{1}{8} \times v_{\text{NO}_2} \times \frac{S}{V} \times \gamma$	$k_{\rm g}, V_{\rm NO_2}, S/V$ , and $\gamma$ are uptake reaction rate of NO <sub>2</sub> by the ground surface (s <sup>-1</sup> ), average molecular velocity (cm s <sup>-1</sup> ), ground surface area density (cm <sup>2</sup> cm <sup>-3</sup> ), and the unitless uptake coefficient (Zhang et al., 2024b).			
Heterogeneous uptake of NO <sub>2</sub> by aerosol surface	$k_{\rm a} = \frac{1}{4} \times v_{\rm NO_2} \times \frac{S}{V} \times \gamma$	$k_{\rm a}, V_{\rm NO_2}, S/V$ , and $\gamma$ are uptake reaction rate of NO <sub>2</sub> by the aerosol surface (s <sup>-1</sup> ), average molecular velocity (cm s <sup>-1</sup> ), aerosol surface area density (cm <sup>2</sup> cm <sup>-3</sup> ), and the unitless uptake coefficient (Zhang et al., 2024b).			
Photolysis of nitrate aerosols	$J_{\text{NO}_3^-} = 120 \times J_{\text{HNO}_3}$	$J_{\mathrm{NO_3^-}}$ and $J_{\mathrm{HNO_3}}$ are the photolysis frequencies of nitrate aerosols and gaseous HNO <sub>3</sub> (Fu et al., 2019). The ratio of 120 is estimated between the measured NO <sub>3</sub> photolysis rate and the default HNO <sub>3</sub> photolysis rate.			
Photo- and dark-oxidation of $NO_X$	$HNO_3 + NO \rightarrow NO_2 + HONO$ $NO_3 + NO \rightarrow 1.98 NO_2 + 0.02 HONO$	Laboratory-based reaction kinetics from Song et al. (2023).			

al. (2024b). In the SOM analysis, seven variables were configured to trace the formation process of HONO. These variables included the homogeneous reaction between NO and OH (NO+OH), NO $_x$  photo-oxidation, NO $_x$  dark-oxidation, primary emissions, the heterogeneous uptake of NO $_2$  by aerosols (Hetero-aerosol), the heterogeneous uptake of NO $_2$  on the ground surface (Hetero-land) and the photol-

ysis of nitrate aerosols (Nitrate-photolysis). The first three sources are categorized as gaseous reaction, while the latter three are categorized as surface reactions. We also quantified two HONO chemical sink pathways: photodissociation of HONO (HONO +  $h\nu$ ) as well as OH-oxidation removal (HONO + OH). Additionally, it should be noted that dry deposition, an important sink for HONO especially at

night, is calculated within the standard WRF-Chem deposition module but was not explicitly tracked in this chemical budget analysis since our focus here was on chemical pathways. Similarly, we also set up the SOM analysis to investigate the formation of OH radicals. Five formation pathways were identified, including the gas-phase reaction between HO<sub>2</sub> and NO (HO<sub>2</sub> + NO), the reaction between atomic oxygen (O<sup>1</sup>D) and H<sub>2</sub>O (O<sup>1</sup>D + H<sub>2</sub>O) initiated by O<sub>3</sub> photolysis (O<sub>3</sub> +  $h\nu \rightarrow$  O<sup>1</sup>D + O<sub>2</sub>), photolysis of HONO (HONO +  $h\nu$ ), photolysis of hydrogen peroxide (H<sub>2</sub>O<sub>2</sub> +  $h\nu$ ), and ozonolysis of VOCs (O<sub>3</sub> + VOCs). All of these chemical reactions are primary sources of OH radical formation except HO<sub>2</sub> + NO, which is generally considered as a secondary conversion (Xue et al., 2025).

## 2.4 Sensitivity experiment designs

Our study also conducted sensitivity experiments to quantify the contribution of oceanic shipping emissions to the formation of HONO in coastal areas, and the contribution of HONO chemistry to the enhancement of ambient O radicals and O<sub>3</sub>. In total, three simulation cases were run, using the same meteorological initial and lateral conditions and continental anthropogenic and biogenic emissions. As listed in Table S1 in the Supplement, the first case was the BASE case, which considered oceanic shipping emissions but did not include the updated HONO sources. The REV case included both oceanic shipping emissions and the updated HONO formation pathways. The "Noship" case denotes a simulation that used an improved HONO source representation but excluded oceanic shipping emissions. By comparing the BASE case (or Noship) with the REV case, we estimated the respective contribution of the updated chemical sources and shipping emissions to HONO formation.

#### 3 Results and discussions

## 3.1 Overview of field observations

Figure 2 shows hourly observations of air pollutants and meteorological parameters at the DZSK site from 1 to 31 May 2024. Generally, HONO concentrations ranged from 0.01 to 1.11 ppbv, with an average of 0.23 ppbv. We compared the HONO measurements at the DZSK site with in situ observations collected from previous studies in China. Table S2 presents a dataset of HONO measurements from 43 studies conducted between 2008 and 2025. It can be concluded that observational studies were intensively carried out in urban areas of the NCP region, particularly in Beijing, where recorded HONO concentrations frequently exceeded 1 ppbv. These higher HONO levels were attributed to abundant NO<sub>x</sub> emissions. By contrast, HONO concentrations were found significantly lower in remote regions. For instance, HONO concentrations ranging from 0.13 to 0.15 ppbv were measured at the summit of Mt. Tai (Jiang et al., 2020; Xue et al., 2022). Studies of coastal regions witnessed HONO concentrations of around 0.50 ppbv (Hu et al., 2022; Zhong et al., 2023). Overall, the HONO levels measured at the DZSK site were much lower than those reported by previous measurements in China. The mean NO<sub>2</sub> concentration during the study period was 3.2 ppbv, due to low NO<sub>x</sub> emissions in this suburban location, which probably contributed to the low HONO concentrations. Meanwhile, the average wind speed was  $2.1 \,\mathrm{m\,s^{-1}}$ , providing a favourable diffusion condition for air pollutants. The prevailing wind direction at the DZSK site was from the northeast, implying a potential contribution from oceanic shipping emissions.

Figure S2 exhibits the diurnal variations of gaseous air pollutants and meteorological parameters. Based on observations of the regional meteorological station in Putian, we categorized any hour with non-zero recorded precipitation into rainy days. On non-rainy days, air temperature and solar radiation were higher, with an apparent peak occurring around midday. Substantial sunlight accelerated the photochemical production of air pollutants such as O<sub>3</sub>. Consequently, concentrations of air pollutants were obviously higher on nonrainy days than on rainy days. At the same time, precipitation also led to the wet deposition of air pollutants. To avoid the influence of precipitation, we focused on the diurnal variation pattern of HONO concentrations excluding rainy days. The maximum hourly HONO concentration at the DZSK site occurred at 14:00 LT on non-rainy days, peaking at 0.38 ppbv. This phenomenon is contrary to the diurnal variations of HONO observed in previous inland measurements. According to Wang et al. (2025), HONO concentrations in inland urban and rural areas typically display the minimum in the afternoon. Despite the decrease in air temperature and radiation after 14:00 LT, the O<sub>3</sub> concentration increased until it reached a daily maximum of 64.8 ppbv at 16:00 LT. The lag of O<sub>3</sub> peak concentration could be attributed to the strengthened AOC conditions resulting from the simultaneous high HONO levels. The chemical production of O<sub>3</sub> is a cumulative process that takes several hours so that O3 levels could remain high even as solar radiation begins to decline, leading to the O<sub>3</sub> peak occurring later in the afternoon. To explore the mechanisms of HONO formation in coastal regions, especially the diurnal peak during the daytime, our study conducted SOM process analyses in the subsequent sections. The potential contribution of shipping emissions to coastal HONO formation was also quantified using sensitivity experiments.

#### 3.2 Evaluations of the numerical model

First, we conducted a model evaluation based on measurements at the DZSK site. Figure 3 demonstrates a comparison between the simulated and observed HONO concentrations. The BASE simulation failed to capture the magnitude and temporal variations of HONO concentrations at the DZSK site. Including multiple HONO formation path-

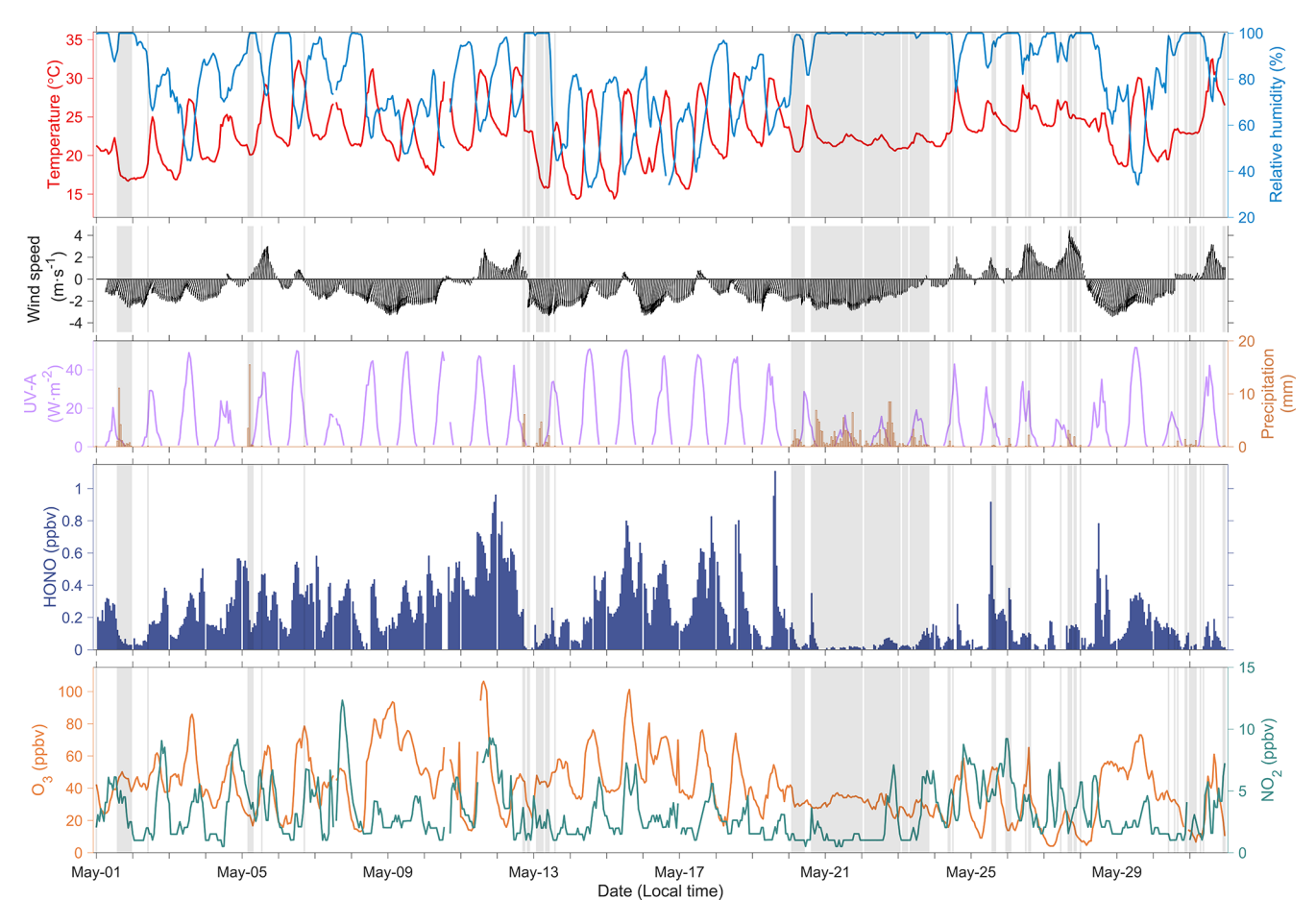
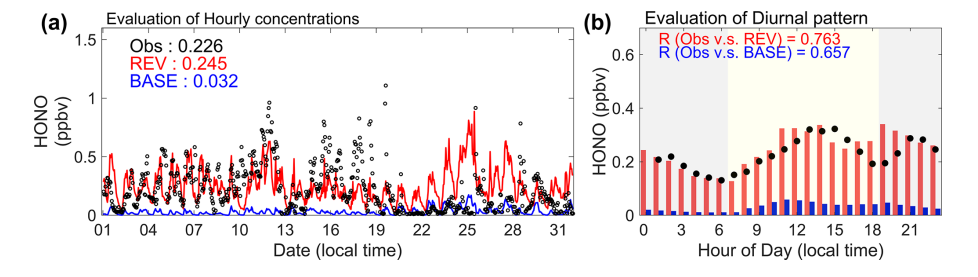


Figure 2. Hourly measurements of meteorological parameters and gaseous air pollutants at the DZSK site during 1–31 May 2024. The shaded areas stand for the period of precipitation.



**Figure 3.** Model evaluations of HONO simulations at the DZSK site in May 2024. Panels (**a**) and (**b**) show comparisons between observations and simulations of hourly and diurnal HONO concentrations, respectively. The red and blue fonts represent the REV and BASE modeling cases, respectively.

ways greatly improved the model performance of HONO (Fig. 3a). The monthly mean HONO concentration increased from 0.03 ppbv (BASE) to 0.25 ppbv (REV). We then applied three statistical metrics to reveal improvements in HONO modeling. The calculation of validation indicators has been elucidated in our previous modeling studies (Zhang et al., 2024b). As summarized in Table 3, while the improvement in the Index of Agreement (IOA, varies from 0 to 1) is modest (from 0.62 to 0.69), the revised model shows a funda-

mental improvement in capturing the magnitude of HONO concentrations. This is demonstrated by the dramatic enhancements in the Normalized Mean Bias (NMB, varies from  $-\infty$  to  $+\infty$ ), which improved from -86% to +8%, and the Root Mean Square Error (RMSE, varies from  $-\infty$  to  $+\infty$ ), which decreased by 21%. While the revised model reasonably reproduced the observed temporal variations in HONO concentrations during the study period, an underestimation existed on 16–18 May, suggesting a potential omis-

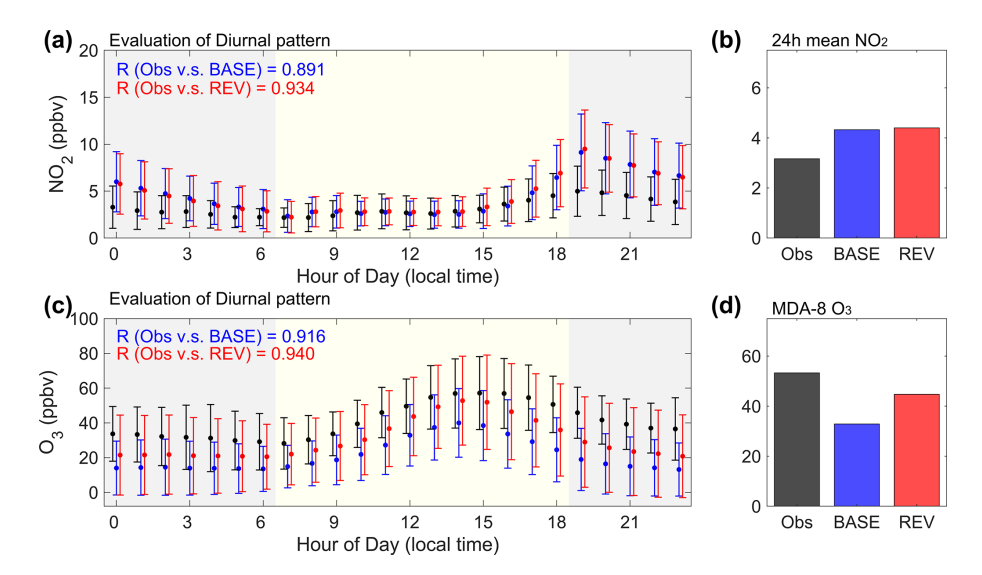


Figure 4. The same as Fig. 3b, but for diurnal variations of NO<sub>2</sub> and O<sub>3</sub> concentrations.

sion of HONO sources. The systematic overestimation during 21-25 May corresponds to a period of continuous rainfall. To provide an evaluation focused on the normal conditions, we also calculated the statistics for non-rainy periods only, where the model performance improved further (IOA = 0.70, NMB = -5%, RMSE = 0.21 ppbv). Simulations including the updated HONO sources more accurately represented the diurnal variation pattern of HONO concentrations. Figure 3b illustrates that the REV case successfully captured the higher HONO concentrations observed around noon. The Pearson's correlation coefficient (R) between the measurements and simulations increased from 0.657 (BASE) to 0.763 (REV). The REV simulation accurately captured the timing of the observed diurnal peak around 14:00 LT, which the BASE case simulates several hours too early. We further show the comparisons between measurements and simulations in terms of diurnal variations of HONO and NO2 on rainy and non-rainy days. As shown in Fig. S3, the daytime HONO concentrations simulated by REV is in good agreement with observations on non-rainy day. However, the model fails to reproduce the observed low concentration levels and the temporal variations of HONO on rainy days, possibly attributed to an underestimated wet removal caused by precipitation. Meanwhile, daytime NO<sub>2</sub> concentrations on rainy days also shows an obvious overestimation, further leading to the higher chemical production of HONO.

The model performance for important precursors and products of HONO chemistry, NO<sub>2</sub> and O<sub>3</sub>, were improved as well. As illustrated in Fig. 4a and c, the diurnal variations of the simulated NO<sub>2</sub> and O<sub>3</sub> concentrations by REV were more consistent with the observed values. The diurnal correlation coefficients between measurements and simulations for NO<sub>2</sub> and O<sub>3</sub> increased by 5 % and 3 %, respectively. At the same time, underestimation of O<sub>3</sub> concentrations in the

**Table 3.** Statistical metrics of evaluating HONO simulations.

	Mean observation (ppbv)	Mean simulation (ppbv)	IOA	NMB	RMSE (ppbv)
BASE	0.23	0.03	0.62	$-86\% \\ +8\%$	0.28
REV	0.23	0.25	0.69		0.22

original model was effectively reduced. The daily maximum O<sub>3</sub> concentration in the revised version (REV) was much closer to the observed value than in the BASE simulation. The estimated maximum daily average 8 h (MDA-8) concentration of O<sub>3</sub> increased from 33 ppbv (BASE) to 45 ppbv (REV), with an observed value of 53 ppbv (Fig. 4d). Accurately characterizing the HONO chemical budget therefore improves the simulation of O<sub>3</sub> concentrations in 3D chemical transport models. The updated HONO chemistry had a limited net impact on NO<sub>2</sub> concentrations due to several competing chemical pathways. Specifically, the consumption of NO<sub>2</sub> by the newly added HONO formation reactions was largely offset by enhanced NO-to-NO<sub>2</sub> conversion from increased OH radicals and altered O<sub>3</sub> titration, resulting in only a minor change in the overall NO<sub>2</sub> budget.

# 3.3 Analyses of HONO formation mechanisms

# 3.3.1 Spatio-temporal characteristics

This study used SOM process analysis to elucidate the mechanisms of HONO formation in Fujian's coastal regions. The analysis focused on the regional average from six coastal cities, as depicted in Fig. 1. The diurnal variations in the chemical production and consumption rates of HONO are presented in Figs. 5a and S4. The maximum HONO produc-

tion rate of over 1.30 ppbv h<sup>-1</sup> occurred during the midday hours (11:00 to 14:00 LT), due to the intensified formation pathways. The HONO consumption rates were primarily influenced by self-photolysis (HONO +  $h\nu$ ) and exhibited a diurnal pattern similar to that of the production rates. The average HONO production rate during the daytime (07:00 to 18:00 LT) was found to be 0.97 ppbv  $h^{-1}$  (Fig. 5b). The SOM analysis revealed that gas-phase and surface reactions contributed equally to daytime HONO formation, accounting for 45 % each. Specifically, the heterogeneous uptake of NO<sub>2</sub> on the ground surface and photo-oxidation of  $NO_x$  emerged as the two principal contributors to HONO formation in coastal regions, with an aggregate contribution of 64 %. In descending order, other sources contributed 16 % (NO + OH), 10 % (primary emissions), 8% (nitrate-photolysis), 2% (heteroaerosol), and less than 1% (NOx dark-oxidation) to daytime HONO formation. Although the heterogeneous uptake of NO<sub>2</sub> on the ground surface was identified as the predominant pathway, its relative importance evidently declined from morning to afternoon (Fig. 5a). This decrease could be attributed to the growing influence of nitrate photolysis, NO + OH, and NO<sub>x</sub> photo-oxidation. The mean nocturnal HONO production rate dropped to  $0.12 \text{ ppbv h}^{-1}$ , reflecting a substantial decline in the intensity of oxidationrelated HONO formation pathways (Fig. 5b). At the same time, HONO consumption rates approached zero at night due to the cessation of photochemical loss mechanisms. Overall, the heterogeneous NO<sub>2</sub> uptake on the ground surface remained the dominant source for nighttime HONO production, accounting for 48 %. In the meantime, the contribution of direct emissions to nocturnal HONO production significantly increased to 17 %.

The mechanisms of HONO formation also proposed spatial heterogeneity. Our study examined HONO formation pathways across different land surfaces, such as forests, grasslands, farmlands, and urban areas (see Table S3). Figure 1b illustrates the spatial distribution of land use information within the study region. In forested areas, SOM analysis indicated that heterogeneous uptake of NO<sub>2</sub> by the ground surface accounted for 45 % of HONO production. This phenomenon is likely linked to the higher density of reactive surface area resulting from the larger leaf area index (LAI) of forested areas (Zhang et al., 2016). In urban areas, however, high NO<sub>x</sub> levels could facilitate greater HONO production through gas-phase reactions involving  $NO_x$ , particularly  $NO_x$  photo-oxidation and NO + OH, which contributed 36 % and 21 %, respectively. The absolute HONO production rates from these two NO<sub>x</sub>-related reactions in urban areas were approximately four times higher than in forests. Direct emissions also contributed significantly to HONO formation (23%) due to intensive NO<sub>x</sub> emissions in urban areas. Since two-thirds of the coastal areas are covered by forests, the regional average contribution of NO2 heterogeneous uptake on the ground surface exceeded that of any NOx-related gasphase oxidation reaction or direct emissions.

Previous investigations have indicated that light-enhanced heterogeneous uptake of NO2 on the ground surface is the dominant source of HONO formation in inland regions (Zhang et al., 2024b). Our diagnostic results in the coastal regions of Fujian support this finding. However, the specific contribution in Fujian (35 %–48 %) was obviously lower than that observed in inland areas (42 %–86 %). Similarly, the contribution from the heterogeneous NO2 uptake on aerosol surfaces (1 %–2 %) was lower than that reported for inland areas (3 %–20 %), because of lower particle concentrations in coastal regions. The WRF-Chem model shows that the average PM<sub>2.5</sub> concentration over the coastal areas of Fujian was  $11.9 \,\mu\mathrm{g}\,\mathrm{m}^{-3}$  during the study period, which is categorized into the clean state and is much lower than the levels in typical inland regions. Moreover, the present study pointed out a greater contribution to HONO formation from NO<sub>x</sub>related gas-phase oxidation reactions than was found in previous studies.

# 3.3.2 Impact of shipping emissions

Furthermore, we conducted sensitivity experiments to evaluate the potential impact of shipping emissions on HONO formation in coastal regions. Figure S5 shows the map of the major shipping routes and ports, which was obtained from the team at Tsinghua University who developed the SEIM model (Wang et al., 2021). The impact of the shipping emissions is based on the atmospheric transport of air pollutants from the upstream region. Specifically, the regional transport is driven by both (SLB). Following the criteria of SLB given by Liu et al. (2025), we identified SLB events over the study region based on the local wind field data exhibited in Fig. 2. The further analysis of wind fields demonstrates that the study area is less affected by the SLB. The impact of shipping emissions on HONO formation was mainly attributed to the transport effect of regional persistent northeasterly wind. It is worth noting that the contribution from shipping emissions to coastal HONO formation is mainly driven by the transport of precursors including  $NO_x$  and  $NO_3^-$ . That is, shipping emissions affect daytime HONO formation via precursor transport followed by local chemical production despite HONO's short atmospheric lifetime. Figure 6 demonstrates the spatial distribution of  $NO_x$ ,  $NO_3^-$ , and HONO concentrations in coastal regions that can be attributed to shipping emissions. As  $NO_x$  is the most important precursor for HONO formation, we first examined the influence of shipping emissions on coastal  $NO_x$  concentrations. The results indicated that shipping emissions caused a net increase of 0.68 ppbv in NO<sub>x</sub> levels across the coastal regions of Fujian, with a clear decrease in gradient from the ocean towards inland areas. It is revealed that shipping emissions contributed 17% to coastal  $NO_x$  concentrations, with a higher contribution in the northern regions than in the middle urban areas. The subsequent rise in  $NO_x$  concentrations led to an increase in nitrate aerosol concentrations, which probably fa-

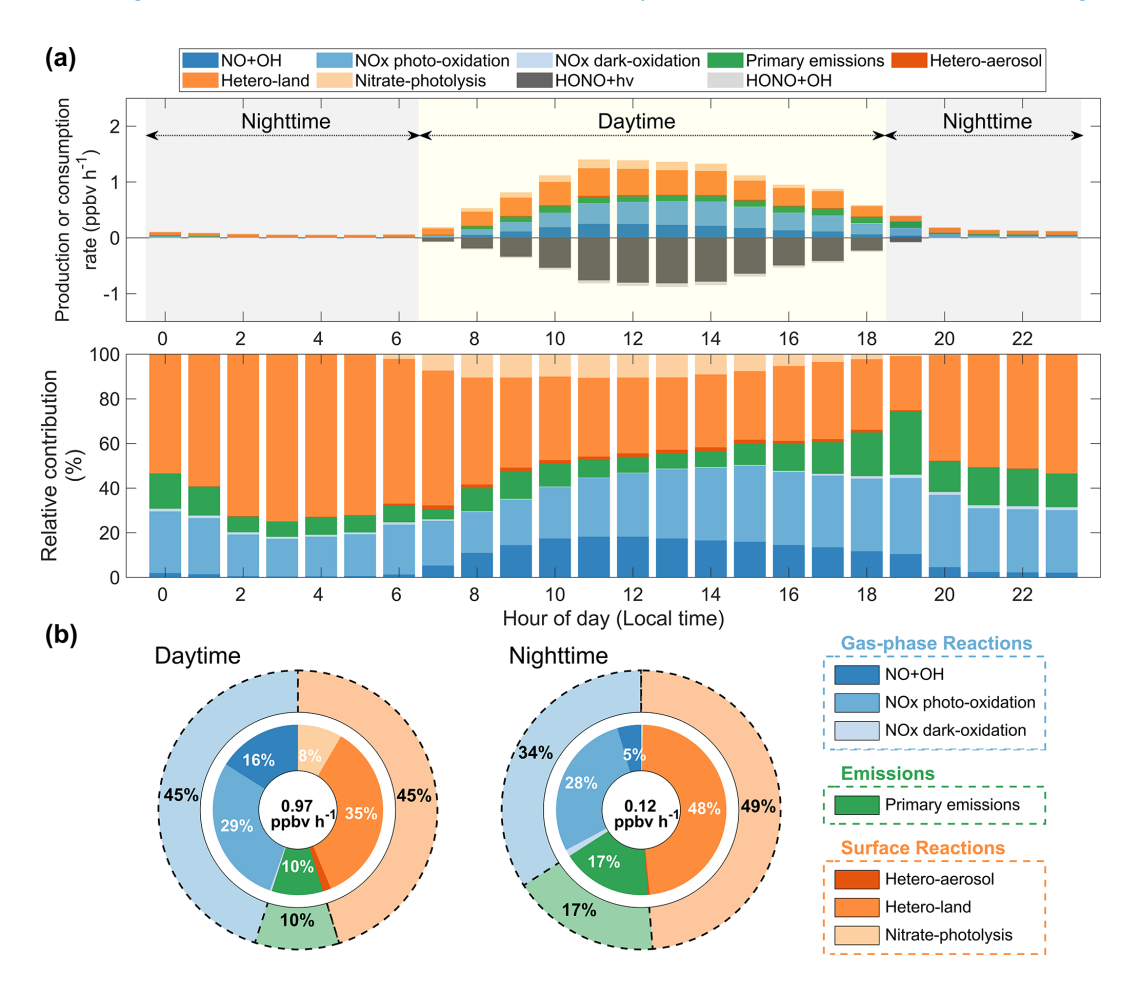


**Figure 5.** Attribution of mechanisms of HONO formation in coastal Fujian in May 2024. Panel (a) shows the diurnal variations in the absolute and relative contributions of seven production and two consumption reactions to the HONO chemical budget. Panel (b) illustrates the contribution of the seven production reactions to daytime and nighttime HONO formation during the study period. The total production rates are labelled in the middle of the pie charts.

cilitated HONO formation. Spatially, shipping emissions induced a net elevation in the average  $NO_3^-$  concentration of  $0.52\,\mu\mathrm{g}\,\mathrm{m}^{-3}$ , accounting for approximately 33% of the total. The spatial distribution of nitrate aerosol concentrations differed from that of  $NO_x$ , with higher levels concentrated mainly in areas with intensive  $NH_3$  emissions. Consequently, HONO levels in the coastal regions of Fujian increased by 36 pptv due to increased precursor concentrations resulting from shipping emissions, representing an 18% relative contribution. Similar to the  $NO_x$  spatial distribution pattern, shipping emissions promoted higher HONO levels in the northern areas of the study region.

As illustrated in Fig. S6, the simulated diurnal range of coastal  $NO_x$  concentrations attributed to shipping emissions was from 0.43 to 0.99 ppbv. This effect was more pronounced during the nighttime hours. Specifically,  $NO_x$  released from the shipping sector preferred to react with  $O_3$  near the ocean surface. As depicted in Fig. S7, the chemical production rates of  $O_3$  during both daytime and nighttime were negative over coastal waters with substantial shipping emissions. This sug-

gests that the transport of NO<sub>x</sub> to coastal regions was probably inhibited. Meanwhile, the O<sub>3</sub> titration effect was more evident during the daytime than at night due to higher shipping emissions, meaning that shipping emissions contributed less to coastal  $NO_x$  during the daytime. Therefore, nitrate aerosols, the products of  $NO_x$  oxidation, exhibited the same diurnal variation pattern as  $NO_x$  with respect to contributions induced by shipping emissions (Fig. S6). Despite the fact that  $NO_x$  and nitrate aerosols contributed by shipping emissions were relatively lower during the daytime, HONO production rates were higher, particularly around noon (Fig. 7). This phenomenon could be attributed to light-dependent reactive pathways that efficiently increased HONO production rates in the presence of sunlight. The mean increased production rate of HONO in coastal regions resulting from shipping emissions during the daytime was  $0.15 \text{ ppbv h}^{-1}$ . Heterogeneous uptake of NO<sub>2</sub> on the ground surface, NO<sub>x</sub> photooxidation, NO+OH, and nitrate photolysis accounted for 39 %, 34 %, 13 %, and 12 % of the total enhancement, respectively. In contrast, HONO production rates attributed to ship-

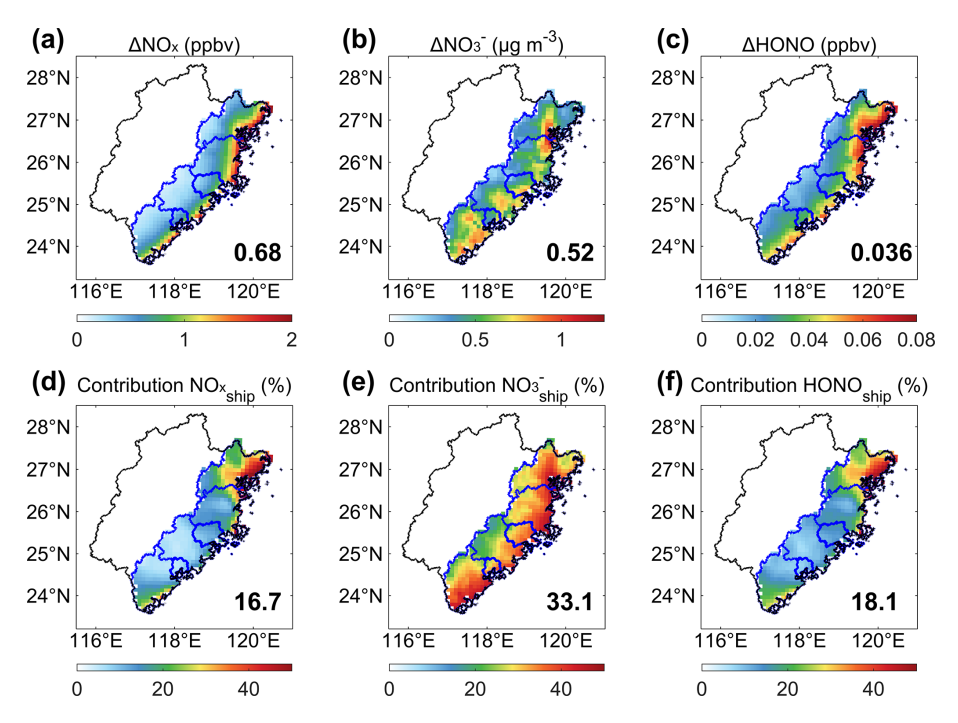
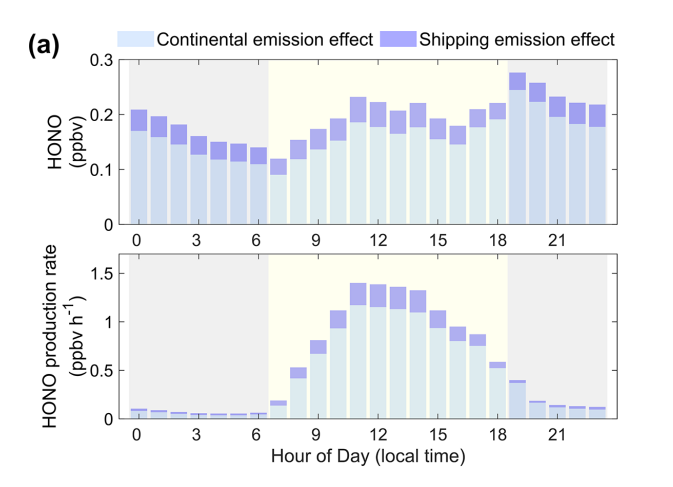


Figure 6. The simulated regional mean effect of shipping emissions on the concentrations of HONO and its precursors, including  $NO_x$  and  $NO_3^-$  aerosols, during the study period. Panels (a)–(c) show the absolute changes, while panels (d)–(f) represent the relative contributions from shipping emissions  $\left(\frac{REV-Noship}{REV}\times100\%\right)$ . The regional average values are marked in the bottom right-hand corner of each panel.

ping emissions were much lower in the evening. However, due to the self-photolysis of HONO, the overall increase in coastal HONO concentrations caused by shipping emissions during the daytime (0.19 ppbv) was close to nighttime levels (0.20 ppbv).

## 3.3.3 Attribution of daytime high HONO concentrations

We subsequently interpreted the causes of the high HONO levels in the coastal regions of Fujian. The captured high HONO concentrations over the study region between 11:00 and 14:00 LT were attributed to the increase in chemical production rates (see Figs. 5a and 7a). There are two main factors. One is a sufficient supply of  $NO_x$  precursors from both continental and shipping emission sources that, even while being at a diurnal minimum around noon, remains ample to fuel the subsequent reactions. The other is an enhanced reaction rate of light-dependent pathways under intense solar radiation. Meanwhile, the aggregate HONO production rate exceeded consumption rates resulting from self-photolysis and OH-oxidation reactions. This contributed to the accumulation of high HONO concentrations. Previous studies concluded that the daytime peak in HONO concentrations was possibly driven by nitrate photolysis (Hu et al., 2022; Wang et al., 2025). However, our attribution analysis inferred that nitrate photolysis was not the dominant factor. Even when a relatively high empirical photolysis frequency of nitrate aerosols (120  $J_{HNO_3}$ ) was applied (Fu et al., 2019; Zhang et al., 2022a), the low nitrate concentration of about  $1.0 \,\mu\mathrm{g}\,\mathrm{m}^{-3}$ only accounted for less than 10% of the overall production rate during the daytime (Fig. S6). This study suggests that heterogeneous NO2 uptake on the ground surface and NO<sub>x</sub> photo-oxidation were the main drivers of HONO formation around noon (11:00 to 14:00 LT), contributing 30 % and 34 %, respectively. The high production rates of these two photo-chemical reactions could be attributed to the persistent abundant solar radiation in coastal areas. Analysis of the spatial distribution patterns of HONO formation mechanisms revealed that the NO<sub>2</sub> heterogeneous uptake reaction on the ground surface was more effective in forests, whereas the photo-oxidation of  $NO_x$  played a more important role in coastal urban areas (Table S3). In addition, HONO photolysis could release OH radicals, facilitating further photooxidation of  $NO_x$ , particularly at noon when the intensity of photochemistry reaches its diurnal peak. We also quantified the contribution of shipping emissions to coastal HONO levels in Fig. 7. We found that  $0.22 \text{ ppbv h}^{-1}$  of the HONO production rate was attributable to shipping emissions around noon, resulting in a 20 % increase in HONO concentrations. These results emphasize the importance of including shipping emissions in the HONO budget near coastal regions.



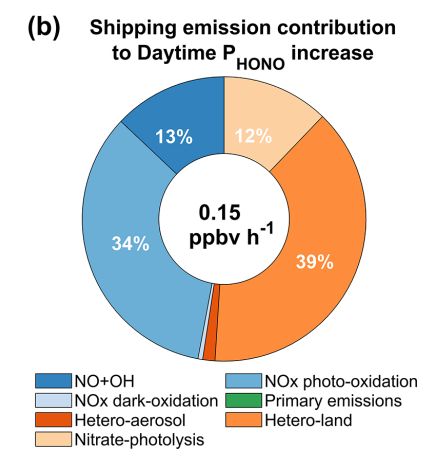


**Figure 7.** The simulated shipping emission contributions to concentrations and formation rates of HONO over the study region. Panel (a) shows the diurnal variations in the effects of continental and shipping emissions on HONO concentrations and formation rates. Panel (b) displays the contribution of shipping emissions to the daytime HONO production rate from different sources.

#### 3.4 Contributions of HONO to ambient oxidants

#### 3.4.1 Enhancement of OH radicals

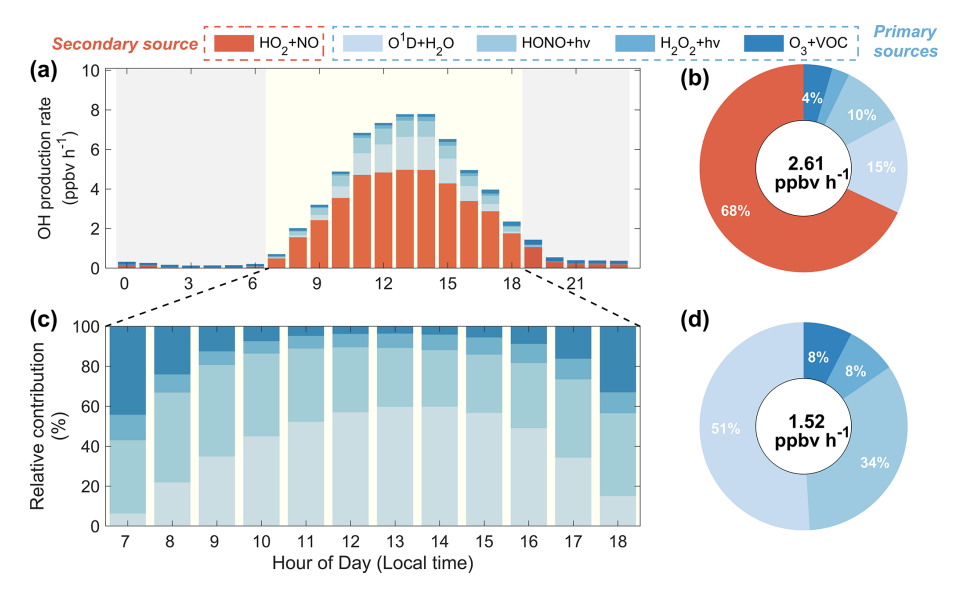
We assessed the role of HONO in OH formation over the coastal regions of Fujian utilizing the SOM process analysis. As illustrated in Fig. 8, the OH production rates from four primary sources and one secondary source are presented. The total OH production rate peaked at 14:00 LT, reaching a maximum value of  $7.78 \text{ ppbv h}^{-1}$  (Fig. 8a). Conversely, OH production rates at night were significantly lower, remaining below 1 ppbv h<sup>-1</sup>. The average daily OH production rate throughout the study period was calculated to be 2.61 ppbv h<sup>-1</sup>. Notably, secondary conversion from the reaction between HO2 and NO was found to dominate OH production, contributing 68 % of the total (Fig. 8b). This fraction is consistent with the results of previous field measurement studies (Yang et al., 2021; Ye et al., 2023). Among primary sources identified, the reaction between O<sup>1</sup>D and H<sub>2</sub>O initiated by O<sub>3</sub> photolysis, and the photolysis of HONO emerged as two significant contributors to OH formation. These two pathways accounted for 15 % and 10 % of the daily OH production rate. Evidently,  $O^1D + H_2O$  and  $HONO + h\nu$  were more influential during daylight hours, with the combined contribution to the OH production rate peaking at 32 % at 13:00 LT.

Figure 8c illustrates the diurnal variations in the relative contributions to OH formation from four primary sources. Model results indicated that the contribution of HONO photolysis to OH formation was notably higher during morning hours. As  $O_3$  concentrations increased, the reaction between  $O^1D$  and  $H_2O$  replaced HONO photolysis as the dominant source for OH formation. This phenomenon has been confirmed by previous observational studies conducted in coastal regions (Hu et al., 2022; Xue et al., 2025). The  $O^1D + H_2O$  reaction reached a maximum contribution of approximately

60 % to OH formation at 14:00 LT. After this peak, the production rates of all reactions decreased due to diminishing sunlight conditions. Generally, the average daytime production rate of OH from primary sources in the coastal regions of Fujian was estimated to be 1.52 ppbv h<sup>-1</sup>. The contributions of the O<sup>1</sup>D + H<sub>2</sub>O, HONO +  $h\nu$ , photolysis of H<sub>2</sub>O<sub>2</sub>, and ozonolysis of VOCs to the primary OH production rate were 51 %, 34 %, 8 %, and 8 %, respectively.

Through sensitivity experiments, we further elucidated the impact of HONO on OH concentrations. As shown in Fig. 9a, the diurnal OH concentrations in the coastal regions of Fujian experienced a remarkable increase due to the improved representation of HONO sources in the WRF-Chem model. Compared to the BASE simulation, the average daytime concentration of OH radicals increased by 57 %. Concurrently, the daily maximum OH concentration rose from  $7.5 \times 10^6$  molec, cm<sup>-3</sup> (BASE) to  $12.1 \times 10^6$  molec, cm<sup>-3</sup> (REV). Measurements of OH radicals were not available in this study for a direct model validation. However, a comprehensive study presenting OH measurements from five field campaigns in China reported that observed noontime peak OH concentrations range from  $4 \times 10^6$  to  $13 \times$ 10<sup>6</sup> molec. cm<sup>-3</sup> across the NCP, YRD, and PRD regions (Ma et al., 2022). The daily maximum OH concentration simulated in our study falls near the upper end of this observed range. While this suggests our simulated value is within the scope of previously measured concentrations in other photochemically active regions of China, we acknowledge that future validation with local measurements is crucial to fully confirm the reasonableness of the updated HONO chemistry. This increase in OH concentration can be attributed to the alteration in OH production rate. The SOM process analysis indicated a 35 % increase in the mean OH production rate.

By integrating sensitivity experiments with the SOM process analysis, we identified two principle factors that con-



**Figure 8.** SOM process analysis of OH production rates in the coastal region of Fujian in May 2024. Panel (a) shows the diurnal variations of OH production rates from five sources. Panel (b) shows the relative contribution of each pathway. Panels (c) and (d) show the specific contribution of the four primary sources to OH formation during the daytime.

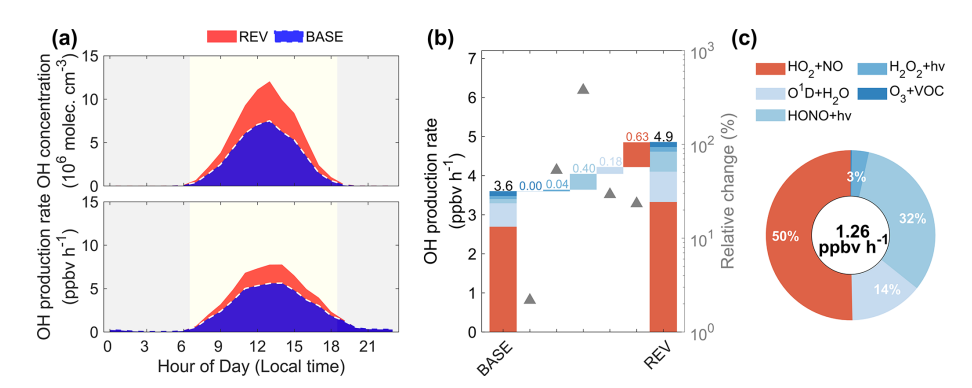


**Figure 9.** Comparisons of HONO concentrations and production rates in coastal Fujian in two simulation cases (BASE and REV). Panel (a) displays the diurnal variations in OH concentrations and production rates. Panel (b) shows the absolute and relative changes in daytime OH formation rates from five chemical sources by comparing the BASE and REV cases. The relative contribution of these sources to the enhancement of the OH production rate is exhibited in panel (c), with the number of increased production rate labelled in the middle of the pie chart.

tributed to the enhancement of OH formation (Fig. 9b). The first factor is the consequence of HONO photolysis, which increased the OH production rate by 0.40 ppbv h $^{-1}$ . Due to the low HONO concentration in the BASE simulation, the contribution of the HONO photolysis to the OH production rate relatively surged by 378 %. The second factor is the promotion of ambient AOC conditions. The increased OH levels then enhanced the formation of oxidative products, including HO<sub>2</sub> radicals, H<sub>2</sub>O<sub>2</sub>, and O<sub>3</sub>. The rise in O<sub>3</sub> further accelerated the generation of O<sup>1</sup>D atom. Consequently, the chemical reactions involving HO<sub>2</sub> + NO, O<sup>1</sup>D + H<sub>2</sub>O, and H<sub>2</sub>O<sub>2</sub> +  $h\nu$  led to increases in the OH production rate of 0.63, 0.18, and 0.04 ppbv h $^{-1}$ , with relative changes of 23 %, 29 %, and 53 %, respectively. The contribution to OH production from

the  $O_3 + VOC$  reaction was negligible as this reaction was more efficient at night and inactive during the daytime. In conclusion, the direct increase in OH formation via HONO photolysis accounted for 32 % of the overall effect attributed to HONO chemistry. The impact of the enhancement in the OH production rate contributed by the other four sources was twice that contributed by the photolysis of HONO (Fig. 9c).

## 3.4.2 Enhancement of O<sub>3</sub> concentration

The sensitivity experiment simultaneously assessed the impact of HONO chemistry on O<sub>3</sub> concentrations. As discussed in Sect. 3.2, the model evaluation of O<sub>3</sub> levels has revealed that the discrepancy between the BASE and REV

cases arises from increased AOC conditions due to the updates of HONO representation. Switching from the BASE simulation to the REV simulation led to an increase in 24hour average O<sub>3</sub> concentration by 9.2 ppbv at the DZSK site, representing a 43 % relative increase. In the coastal regions of Fujian, the regional mean absolute enhancement of O<sub>3</sub> concentration was 9.9 ppbv, corresponding to a relative increase of 44%, comparable to the findings at DZSK. Moreover, we compared the simulated absolute and relative alternations in O<sub>3</sub> concentrations attributable to HONO chemistry with the results of sensitivity experiments utilizing 3D chemical transport models obtained from previous studies. The related comparisons are summarized in Table 4. Most of the referenced studies referenced were conducted in densely populated areas in eastern China. The compilation suggests that the absolute increase in O<sub>3</sub> concentration driven by HONO chemistry across most studies was approximately 10 ppbv and consistent with the value presented by this study. However, the relative enhancement of O<sub>3</sub> levels in this study (43 %–44 %) was significantly higher than the range reported in previous studies (12 %–38 %), with the exception of the outlier proposed by Fu et al. (2019). While the relative enhancement of 44 % appears high, it is largely a consequence of correcting the significant underestimation of O<sub>3</sub> in the BASE simulation. The absolute increase is in line with the values reported by many previous modeling studies, emphasizing the importance of including complete HONO sources as possible in 3D models to accurately simulate coastal O<sub>3</sub>.

## 3.5 Uncertainties

Several uncertainties exist in the HONO simulations presented in this study, firstly related to the parameterization of key chemical pathways. These are mainly concentrated in the heterogeneous uptake coefficients and the nitrate aerosol photolysis rate. For the nitrate photolysis frequency, Zhang et al. (2022a) summarized that this value is approximately 1-3 orders of magnitude higher than the photolysis frequency of HNO<sub>3</sub>. Our study adopted a median value of this range  $(120 J_{HNO_3})$ , which was inferred based on aircraft measurements in the North Atlantic marine boundary layer and has been widely used in previous studies (Fu et al., 2019; Ye et al., 2016; Zhang et al., 2021). For the heterogeneous uptake of NO<sub>2</sub> on solid surfaces, the dimensionless uptake coefficient typically ranges from  $10^{-6}$  to  $10^{-3}$ . For the ground surface, we also applied a representative median value, with this coefficient varying from a nighttime baseline in the  $10^{-6}$  range up to a maximum of  $6 \times 10^{-5}$  under peak sunlight (Wang et al., 2025). For the aerosol surfaces, we set the maximum daytime value to  $1 \times 10^{-3}$ , an upper limit reported in the literature, which carries a potential uncertainty. To quantitatively assess the impact of this choice, we conducted an additional sensitivity analysis where the uptake coefficient  $\gamma_a$  was reduced to  $1 \times 10^{-4}$  and  $1 \times 10^{-5}$ , respectively. To minimize the computational burden, these simulations were performed for the first seven days of our study period. As shown in Table S4, model results show that while lowering the  $\gamma_a$  value does lead to a corresponding decrease in the HONO production rate from the heterogeneous uptake of NO<sub>2</sub> by aerosols, the impact on the overall HONO budget is negligible. The average daytime HONO concentration decreased by less than 2 pptv, a relative change of less than 1 %. This finding provides quantitative support for our argument that due to the low aerosol abundance in this coastal region, the heterogeneous aerosol pathway contributes minimally to HONO formation, regardless of the precise  $\gamma_a$  value. Consequently, the responses in O<sub>3</sub> and OH concentrations were also minimal. This confirms that our use of  $1 \times 10^{-3}$  as an upper-limit for  $\gamma_a$  is a reasonable choice and does not compromise the main conclusions of our study.

Secondly, we used an empirical HONO /  $NO_x$  value of 1.45 % to estimate the direct HONO emissions from the fuel combustion process. This value was derived from long-term in situ measurements in coastal regions and proposed by Hu et al. (2022). We applied this value to describe fresh HONO emissions from ships. However, Ke et al. (2025) have pointed out that the same ratio of HONO to  $NO_x$  may not be applicable to mobile sources, including mobile machinery, ships, and aircraft. The ratios of HONO to NOx were examined to be 0.8 %-6.0 % and 2.3 % for aircraft and offroad mobile machinery, respectively. Currently, there are no direct measurements of freshly emitted HONO from shipping. Therefore, further observations and experiments are required to constrain HONO emissions from ships. In addition to mobile emissions for HONO from combustion processes, the soil volatilization could be another important contributor to ambient HONO (Tan et al., 2023; Wu et al., 2022), especially when there are large areas of cropland and agricultural activities. The neglect of soil HONO emissions may introduce some uncertainties in the HONO simulation in this study.

Thirdly, the ocean surface may affect HONO formation in other ways. Zha et al. (2014) observed significant evidence suggesting that the ocean was a nonnegligible contributor to coastal HONO production. Consequently, Zhang et al. (2016) parameterized this reaction as heterogeneous uptake by the ocean surface in the WRF-Chem model using a simplified formula. Additionally, an observational study proposed that seawater could increase the solubility of HONO under certain conditions, indicating that the ocean surface could act as a sink for atmospheric HONO (Crilley et al., 2021; Wang et al., 2025). However, the source or sink effect of the ocean on HONO remains a controversial topic. Further studies on this theory and the relevant parameterization are needed in the future.

Period	Region	Model	Absolute	Relative	References
			$\Delta O_3$	$\Delta O_3$	
			(ppbv)	(%)	
25–31 August 2011	Hong Kong	WRF-Chem	4.0	12	Zhang et al. (2016)
26 June to 7 July 2014	East China	WRF-Chem	2.9-6.2	6–13	Zhang et al. (2017)
4–8 January 2017	Heshan, PRD	CMAQ	24.0	70	Fu et al. (2019)
22–31 July 2016	NCP		13.0	_	
7–13 July 2013	YRD	WRF-Chem	14.7	_	Guo et al. (2020)
18–31 October 2015	PRD		10.7	_	
3 December 2015 to 14 January 2016	Xi'an	WRF-Chem	_	22	Li et al. (2022)
1 March to 31 May 2016	an	TABLE CI	7.9	17	Zhang et al. (2022b)
1 July to 30 September 2016	NCP	WRF-Chem	8.9	16	
8–22 June 2017	NCP	WRF-Chem	26.1	38	Song et al. (2023)
1–7 June 2017			6.9	16	
8–13 June 2017	NCP	WRF-Chem	9.5	20	Ran et al. (2024)
14–21 June 2017			11.2	22	
24–27 March 2019	Nanjing, YRD	WRF-Chem	8.9	28	Zhang et al. (2024b)
1 21 M 2024	DZSK Coastal areas	WRF-Chem	9.2	43	This study
1–31 May 2024			9.9	44	

Table 4. Compilation of contributions of HONO photolysis to enhancement of O<sub>3</sub> concentrations from previous studies.

## 4 Conclusions

This study investigated the mechanisms of HONO chemical formation and its impact on the enhancement of ambient oxidants in coastal Fujian of southeastern China. Based on continuous in situ measurements over a one-month period at a suburban site, we found that the observed HONO showed an unexpected diurnal variation pattern with higher levels measured at noon, contrary to an obvious daytime minimum reported by extensive previous studies focusing on inland areas. Using a revised WRF-Chem model incorporating updates to multiple sources of HONO, including direct emissions,  $NO_2$  heterogeneous uptake by solid surfaces, nitrate photolysis, and the photo- and dark-oxidation of  $NO_x$ , we were able to reasonably reproduce the magnitude and temporal variation of HONO concentrations, especially the higher values observed at noon.

To better understand the mechanisms of HONO formation in the coastal regions of Fujian, we subsequently utilized the SOM process analysis. In general, heterogeneous uptake of  $NO_2$  on the ground surface and  $NO_x$  photo-oxidation were two principal contributors to HONO formation, contributing 35 %–48 % and 28 %–29 %, respectively. From 11:00 to 14:00 LT, these two light-dependent reactive pathways led to rapid HONO production rates and offset the effect of lower precursor concentrations, accounting for 64 % of the total. Notably, the formed HONO could release OH radicals by self-photolysis, thereby facilitating  $NO_x$  photo-oxidation.

Spatially, model results suggested that the heterogeneous uptake of  $NO_2$  on the ground surface was more important in forest areas due to the higher density of reactive surface area. In urban areas, high  $NO_x$  levels resulted in more HONO production through gas-phase oxidation reactions.

Our study highlights that while the primary daytime loss mechanism for HONO is self-photodissociation in both coastal and highly polluted inland urban areas, their formation mechanisms exhibit significant discrepancies. Previous studies in inland areas often identify the heterogeneous uptake of NO<sub>2</sub> on ground surfaces as the dominant source with the maximum contribution up to 86% (Zhang et al., 2024b). Our findings in coastal Fujian reveal that the heterogeneous uptake on the ground surface and photo-oxidation of NO? were found to be equally crucial contributors. Furthermore, the contribution from heterogeneous uptake of NO<sub>2</sub> on aerosol surfaces, which can be significant in a typical urban environment, was found to be negligible (1%–2%) in coastal areas due to much lower aerosol concentrations.

We also assessed the impact of shipping emissions on HONO formation in coastal regions by carrying out sensitivity experiments. The model results indicated that shipping emissions contributed to regional increases in  $NO_x$  and  $NO_3^-$  by 17% and 33%, consequently elevating the average HONO concentration by 18%. The contribution of shipping emissions to HONO decreased from coastal to inland areas. The increased HONO concentrations could be explained by the enhanced production rates. Shipping emissions con-

tributed more evidently to HONO production rates during the daytime, with heterogeneous uptake of  $NO_2$  on the ground surface,  $NO_x$  photo-oxidation, NO + OH, and nitrate photolysis accounting for 39 %, 34 %, 13 %, and 12 % of the total enhancement, respectively.

This study identifies photochemical-driven processes as the dominant driver of the midday HONO peak in May, a late spring period characterized by abundant solar radiation. Given a more intense solar radiation in summer, it is possible that the daytime HONO formation would be even more pronounced. Whereas in winter, the contribution from these photochemical pathways would likely diminish, potentially leading to a less distinct diurnal pattern where other sources, such as direct emissions, could become relatively more important. Furthermore, the mechanisms discussed in this study might be applicable to other mid-latitude coastal regions worldwide that have similar conditions including  $NO_x$  precursor sources from shipping emissions and abundant solar radiation. Coastal areas such as the Mediterranean region, the coast of California, and monsoon zones in East Asia may therefore experience similar HONO diurnal variations. To shed more light on coastal HONO chemistry, future longterm, multi-seasonal measurement campaigns in a wider variety of coastal environments are still in need.

Including good HONO source representation significantly led to the rise in concentrations of OH radicals and O<sub>3</sub>. The SOM process analysis revealed that photolysis of HONO accounted for 34 % of primary OH formation. Meanwhile, this chemical reactive pathway played a more important role in OH formation during the morning rush hours. A sensitivity experiment showed that the diurnal peak of OH levels increased by 61 % due to improved representation of HONO sources in the WRF-Chem model. Adjoint SOM analysis of two modeling cases involving BASE and REV further elucidated that only 32 % of the increased OH production rate was explained by the direct influence of HONO photolysis; the remainder was contributed by other reactions, including  $HO_2 + NO$ ,  $O^1D + H_2O$ , and  $H_2O_2 + h\nu$ , due to ambient increased AOC conditions. Consequently, the average O<sub>3</sub> concentration increased by 44 % in the coastal regions of Fujian, a much more significant elevation than in previous studies.

Overall, the present study highlights the critical importance of characterizing HONO's formation mechanisms and environmental impacts in coastal regions. Moreover, our study discussed the potential uncertainties regarding HONO simulations in coastal regions, including those arising from the parameterizations of heterogeneous uptake and nitrate photolysis, the estimates of direct emissions from shipping activities, and the unknown impact of the ocean surface. Therefore, the representative model parameterizations concerning the complicated formation processes of HONO should be continuously developed and coupled into numerical models in the future.

Data availability. The source codes of the WRF-Chem model are publicly available on the official website of GitHub (https: //github.com/wrf-model/WRF). Meteorological input data for modeling are archived at https://rda.ucar.edu/ (last access: 28 October 2025), with the product codes of d083002, d461000 and d351000 for FNL reanalysis dataset, surface and upper weather observations. Anthropogenic emission inventories of MEIC and SEIM developed by Tsinghua University can be downloaded from the website of http://meicmodel.org.cn/ (last access: 28 October 2025). Other observational and modeling data used in this study are archived on the Figshare platform at https://doi.org/10.6084/m9.figshare.29827070.v1 (Zhang, 2025).

**Supplement.** The supplement related to this article is available online at https://doi.org/10.5194/acp-25-16797-2025-supplement.

**Author contributions.** XH conceptualized and supervised the study. HRZ performed the model simulations. CYY, SHW and ELN provided the measurement data in Fujian. HRZ and XH analyzed the data and interpreted the results with the help from TYL. HRZ wrote the original manuscript. XH and HRZ revised and edited this paper with contributions from all other co-authors.

**Competing interests.** The contact author has declared that none of the authors has any competing interests.

**Disclaimer.** Publisher's note: Copernicus Publications remains neutral with regard to jurisdictional claims made in the text, published maps, institutional affiliations, or any other geographical representation in this paper. While Copernicus Publications makes every effort to include appropriate place names, the final responsibility lies with the authors. Views expressed in the text are those of the authors and do not necessarily reflect the views of the publisher.

**Acknowledgements.** We are grateful for support from the Comprehensive Observation and Research Project on Atmospheric Pollution in the Meizhou Bay Region and the New Cornerstone Science Foundation through the XPLORER PRIZE. We also thank the editors and three reviewers for their work.

Financial support. This research has been supported by the Ministry of Science and Technology of the People's Republic of China (2022YFC3701101), the National Natural Science Foundation of China (42293322 and 424B2040), the Natural Science Foundation of Fujian Province (2022J01518 and 2024J01168), the Comprehensive Observation and Research Project on Atmospheric Pollution in the Meizhou Bay Region and the New Cornerstone Science Foundation through the XPLORER PRIZE.

**Review statement.** This paper was edited by Andrea Pozzer and reviewed by three anonymous referees.

# **References**

- Acker, K., Febo, A., Trick, S., Perrino, C., Bruno, P., Wiesen, P., Möller, D., Wieprecht, W., Auel, R., Giusto, M., Geyer, A., Platt, U., and Allegrini, I.: Nitrous acid in the urban area of Rome, Atmos. Environ., 40, 3123–3133, https://doi.org/10.1016/j.atmosenv.2006.01.028, 2006.
- Carter, W. P. L.: Documentation of the SAPRC-99 Chemical Mechanism for VOC Reactivity Assessment, Contracts 92-329 and 95-308, Report to the California Air resources Board, https://doi.org/10.5281/zenodo.12600705, 2000.
- Chen, F. and Dudhia, J.: Coupling and advanced land surface-hydrology model with the Penn State-NCAR MM5 modeling system. Part I: Model implementation and sensitivity, Mon. Weather Rev., 129, 569–585, https://doi.org/10.1175/1520-0493(2001)129<69:CAALSH%253>.CO;2, 2001.
- Crilley, L. R., Kramer, L. J., Pope, F. D., Reed, C., Lee, J. D., Carpenter, L. J., Hollis, L. D. J., Ball, S. M., and Bloss, W. J.: Is the ocean surface a source of nitrous acid (HONO) in the marine boundary layer?, Atmos. Chem. Phys., 21, 18213–18225, https://doi.org/10.5194/acp-21-18213-2021, 2021.
- Dai, J. and Wang, T.: Impact of international shipping emissions on ozone and PM<sub>2.5</sub> in East Asia during summer: the important role of HONO and ClNO<sub>2</sub>, Atmos. Chem. Phys., 21, 8747–8759, https://doi.org/10.5194/acp-21-8747-2021, 2021.
- Dunlea, E. J., Herndon, S. C., Nelson, D. D., Volkamer, R. M., San Martini, F., Sheehy, P. M., Zahniser, M. S., Shorter, J. H., Wormhoudt, J. C., Lamb, B. K., Allwine, E. J., Gaffney, J. S., Marley, N. A., Grutter, M., Marquez, C., Blanco, S., Cardenas, B., Retama, A., Ramos Villegas, C. R., Kolb, C. E., Molina, L. T., and Molina, M. J.: Evaluation of nitrogen dioxide chemiluminescence monitors in a polluted urban environment, Atmos. Chem. Phys., 7, 2691–2704, https://doi.org/10.5194/acp-7-2691-2007, 2007.
- Finlayson-Pitts, B. J., Wingen, L. M., Sumner, A. L., Syomin, D., and Ramazan, K. A.: The heterogeneous hydrolysis of NO<sub>2</sub> in laboratory systems and in outdoor and indoor atmospheres: An integrated mechanism, Phys. Chem. Chem. Phys., 5, 223–242, https://doi.org/10.1039/B208564J, 2003.
- Fu, X., Wang, T., Zhang, L., Li, Q., Wang, Z., Xia, M., Yun, H., Wang, W., Yu, C., Yue, D., Zhou, Y., Zheng, J., and Han, R.: The significant contribution of HONO to secondary pollutants during a severe winter pollution event in southern China, Atmos. Chem. Phys., 19, 1–14, https://doi.org/10.5194/acp-19-1-2019, 2019.
- George, C., Ammann, M., D'Anna, B., Donaldson, D. J., and Nizkorodov, S. A.: Heterogeneous Photochemistry in the Atmosphere, Chem. Rev., 115, 4218–4258, https://doi.org/10.1021/cr500648z, 2015.
- Grell, G. A. and Dévényi, D.: A generalized approach to parameterizing convection combining ensemble and data assimilation techniques, Geophys. Res. Lett., 29, https://doi.org/10.1029/2002GL015311, 2002.
- Grell, G. A., Peckham, S. E., Schmitz, R., McKeen, S. A., Frost, G., Skamarock, W. C., and Eder, B.: Fully coupled "online" chemistry within the WRF model, Atmos. Environ., 39, 6957–6975, https://doi.org/10.1016/j.atmosenv.2005.04.027, 2005.

- Guenther, A., Karl, T., Harley, P., Wiedinmyer, C., Palmer, P. I., and Geron, C.: Estimates of global terrestrial isoprene emissions using MEGAN (Model of Emissions of Gases and Aerosols from Nature), Atmos. Chem. Phys., 6, 3181–3210, https://doi.org/10.5194/acp-6-3181-2006, 2006.
- Guo, Y., Zhang, J., An, J., Qu, Y., Liu, X., Sun, Y., and Chen, Y.: Effect of vertical parameterization of a missing daytime source of HONO on concentrations of HONO, O3 and secondary organic aerosols in eastern China, Atmos. Environ., 226, 117208, https://doi.org/10.1016/j.atmosenv.2019.117208, 2020.
- Hong, S.-Y., Noh, Y., and Dudhia, J.: A New Vertical Diffusion Package with an Explicit Treatment of Entrainment Processes, Mon. Weather Rev., 134, 2318–2341, https://doi.org/10.1175/MWR3199.1, 2006.
- Hu, B., Duan, J., Hong, Y., Xu, L., Li, M., Bian, Y., Qin, M., Fang, W., Xie, P., and Chen, J.: Exploration of the atmospheric chemistry of nitrous acid in a coastal city of southeastern China: results from measurements across four seasons, Atmos. Chem. Phys., 22, 371–393, https://doi.org/10.5194/acp-22-371-2022, 2022.
- Iacono, M. J., Delamere, J. S., Mlawer, E. J., Shephard, M. W., Clough, S. A., and Collins, W. D.: Radiative forcing by long-lived greenhouse gases: Calculations with the AER radiative transfer models, J. Geophys. Res.-Atmos., 113, https://doi.org/10.1029/2008JD009944, 2008.
- Jiang, Y., Xue, L., Gu, R., Jia, M., Zhang, Y., Wen, L., Zheng, P., Chen, T., Li, H., Shan, Y., Zhao, Y., Guo, Z., Bi, Y., Liu, H., Ding, A., Zhang, Q., and Wang, W.: Sources of nitrous acid (HONO) in the upper boundary layer and lower free troposphere of the North China Plain: insights from the Mount Tai Observatory, Atmos. Chem. Phys., 20, 12115–12131, https://doi.org/10.5194/acp-20-12115-2020, 2020.
- Jiang, Y., Hoffmann, E. H., Tilgner, A., Aiyuk, M. B. E., Andersen, S. T., Wen, L., van Pinxteren, M., Shen, H., Xue, L., Wang, W., and Herrmann, H.: Insights Into  $NO_X$  and HONO Chemistry in the Tropical Marine Boundary Layer at Cape Verde During the MarParCloud Campaign, J. Geophys. Res.-Atmos., 128, e2023JD038865, https://doi.org/10.1029/2023JD038865, 2023.
- Jiang, Y., Xia, M., Xue, L., Wang, X., Zhong, X., Liu, Y., Kulmala, M., Ma, T., Wang, J., Wang, Y., Gao, J., and Wang, T.: Quantifying HONO Production from Nitrate Photolysis in a Polluted Atmosphere, Environ. Sci. Technol., 58, 14361–14371, https://doi.org/10.1021/acs.est.4c06061, 2024.
- Jiménez, P. A., Dudhia, J., González-Rouco, J. F., Navarro, J., Montávez, J. P., and García-Bustamante, E.: A revised scheme for the WRF surface layer formulation, Mon. Weather Rev., 140, 898–918, https://doi.org/10.1175/MWR-D-11-00056.1, 2012.
- Ke, J., Yang, X., Lu, K., Fu, M., Wang, Y., Yin, H., and Ding, Y.: Overlooked Underestimation of Mobile Sources Posing a Pronounced Imbalance in the HONO Budget, Environ. Sci. Technol., 59, 5875–5877, https://doi.org/10.1021/acs.est.5c02684, 2025.
- Kim, K., Han, K. M., Song, C. H., Lee, H., Beardsley, R., Yu, J., Yarwood, G., Koo, B., Madalipay, J., Woo, J.-H., and Cho, S.: An investigation into atmospheric nitrous acid (HONO) processes in South Korea, Atmos. Chem. Phys., 24, 12575–12593, https://doi.org/10.5194/acp-24-12575-2024, 2024.

- Kleffmann, J., Gavriloaiei, T., Hofzumahaus, A., Holland, F., Koppmann, R., Rupp, L., Schlosser, E., Siese, M., and Wahner, A.: Daytime formation of nitrous acid: A major source of OH radicals in a forest, Geophys. Res. Lett., 32, https://doi.org/10.1029/2005GL022524, 2005.
- Kurtenbach, R., Becker, K. H., Gomes, J. A. G., Kleffmann, J., Lörzer, J. C., Spittler, M., Wiesen, P., Ackermann, R., Geyer, A., and Platt, U.: Investigations of emissions and heterogeneous formation of HONO in a road traffic tunnel, Atmos. Environ., 35, 3385–3394, https://doi.org/10.1016/S1352-2310(01)00138-8, 2001.
- Li, M., Zhang, Q., Kurokawa, J., Woo, J.-H., He, K., Lu, Z., Ohara, T., Song, Y., Streets, D. G., Carmichael, G. R., Cheng, Y., Hong, C., Huo, H., Jiang, X., Kang, S., Liu, F., Su, H., and Zheng, B.: MIX: a mosaic Asian anthropogenic emission inventory under the international collaboration framework of the MICS-Asia and HTAP, Atmos. Chem. Phys., 17, 935–963, https://doi.org/10.5194/acp-17-935-2017, 2017.
- Li, X., Bei, N., Wu, J., Wang, R., Liu, S., Liu, L., Jiang, Q., Tie, X., Molina, L. T., and Li, G.: Heterogeneous HONO formation deteriorates the wintertime particulate pollution in the Guanzhong Basin, China, Environ. Pollut., 303, 119157, https://doi.org/10.1016/j.envpol.2022.119157, 2022.
- Lin, Y.-L., Farley, R. D., and Orville, H. D.: Bulk Parameterization of the Snow Field in a Cloud Model, Journal of Applied Meteorology and Climatology, 22, 1065–1092, 1983.
- Liu, C., Wang, H., Li, L., Chen, X., Lu, X., and Fan, S.: Impacts of sea-land breeze on the coastal ozone in the Pearl River Delta, China, J. Environ. Sci., https://doi.org/10.1016/j.jes.2025.08.037, in press, 2025.
- Liu, H., Fu, M., Jin, X., Shang, Y., Shindell, D., Faluvegi, G., Shindell, C., and He, K.: Health and climate impacts of oceangoing vessels in East Asia, Nat. Clim. Change, 6, 1037–1041, https://doi.org/10.1038/nclimate3083, 2016.
- Liu, Y., Lu, K., Li, X., Dong, H., Tan, Z., Wang, H., Zou, Q., Wu, Y., Zeng, L., Hu, M., Min, K.-E., Kecorius, S., Wiedensohler, A., and Zhang, Y.: A Comprehensive Model Test of the HONO Sources Constrained to Field Measurements at Rural North China Plain, Environ. Sci. Technol., 53, 3517–3525, https://doi.org/10.1021/acs.est.8b06367, 2019.
- Ma, X., Tan, Z., Lu, K., Yang, X., Chen, X., Wang, H., Chen, S., Fang, X., Li, S., Li, X., Liu, J., Liu, Y., Lou, S., Qiu, W., Wang, H., Zeng, L., and Zhang, Y.: OH and HO<sub>2</sub> radical chemistry at a suburban site during the EXPLORE-YRD campaign in 2018, Atmos. Chem. Phys., 22, 7005–7028, https://doi.org/10.5194/acp-22-7005-2022, 2022.
- Meusel, H., Kuhn, U., Reiffs, A., Mallik, C., Harder, H., Martinez, M., Schuladen, J., Bohn, B., Parchatka, U., Crowley, J. N., Fischer, H., Tomsche, L., Novelli, A., Hoffmann, T., Janssen, R. H. H., Hartogensis, O., Pikridas, M., Vrekoussis, M., Bourtsoukidis, E., Weber, B., Lelieveld, J., Williams, J., Pöschl, U., Cheng, Y., and Su, H.: Daytime formation of nitrous acid at a coastal remote site in Cyprus indicating a common ground source of atmospheric HONO and NO, Atmos. Chem. Phys., 16, 14475–14493, https://doi.org/10.5194/acp-16-14475-2016, 2016.

- Nakashima, Y., Sadanaga, Y., Saito, S., Hoshi, J., and Ueno, H.: Contributions of vehicular emissions and secondary formation to nitrous acid concentrations in ambient urban air in Tokyo in the winter, Sci. Total Environ., 592, 178–186, https://doi.org/10.1016/j.scitotenv.2017.03.122, 2017.
- Oswald, R., Behrendt, T., Ermel, M., Wu, D., Su, H., Cheng, Y., Breuninger, C., Moravek, A., Mougin, E., Delon, C., Loubet, B., Pommerening-Röser, A., Sörgel, M., Pöschl, U., Hoffmann, T., Andreae, M. O., Meixner, F. X., and Trebs, I.: HONO Emissions from Soil Bacteria as a Major Source of Atmospheric Reactive Nitrogen, Science, 341, 1233–1235, https://doi.org/10.1126/science.1242266, 2013.
- Ran, H., An, J., Zhang, J., Huang, J., Qu, Y., Chen, Y., Xue, C., Mu, Y., and Liu, X.: Impact of soil–atmosphere HONO exchange on concentrations of HONO and O<sub>3</sub> in the North China Plain, Sci. Total Environ., 928, 172336, https://doi.org/10.1016/j.scitotenv.2024.172336, 2024.
- Ren, C., Huang, X., Wang, Y., Zhang, L., Zhou, X., Sun, W., Zhang, H., Liu, T., Ding, A., and Wang, T.: Enhanced Soil Emissions of Reactive Nitrogen Gases by Fertilization and Their Impacts on Secondary Air Pollution in Eastern China, Environ. Sci. Technol., 59, 5119–5130, https://doi.org/10.1021/acs.est.4c12324, 2025.
- Sarwar, G., Roselle, S. J., Mathur, R., Appel, W., Dennis, R. L., and Vogel, B.: A comparison of CMAQ HONO predictions with observations from the Northeast Oxidant and Particle Study, Atmos. Environ., 42, 5760–5770, https://doi.org/10.1016/j.atmosenv.2007.12.065, 2008.
- Seinfeld, J. H. and Pandis, S. N.: Atmospheric Chemistry and Physics: From Air Pollution to Climate Change, John Wiley & Sons, Hoboken, New Jersey, ISBN 978-1-118-94740-1, 2016.
- Song, M., Zhao, X., Liu, P., Mu, J., He, G., Zhang, C., Tong, S., Xue, C., Zhao, X., Ge, M., and Mu, Y.: Atmospheric NO<sub>x</sub> oxidation as major sources for nitrous acid (HONO), Npj Clim. Atmos. Sci., 6, 30, https://doi.org/10.1038/s41612-023-00357-8, 2023.
- Stutz, J., Oh, H.-J., Whitlow, S. I., Anderson, C., Dibb, J. E., Flynn, J. H., Rappenglück, B., and Lefer, B.: Simultaneous DOAS and mist-chamber IC measurements of HONO in Houston, TX, Atmos. Environ., 44, 4090–4098, https://doi.org/10.1016/j.atmosenv.2009.02.003, 2010.
- Su, H., Cheng, Y., Oswald, R., Behrendt, T., Trebs, I., Meixner, F. X., Andreae, M. O., Cheng, P., Zhang, Y., and Pöschl, U.: Soil Nitrite as a Source of Atmospheric HONO and OH Radicals, Science, 333, 1616–1618, https://doi.org/10.1126/science.1207687, 2011.
- Sun, L., Chen, T., Jiang, Y., Zhou, Y., Sheng, L., Lin, J., Li, J., Dong, C., Wang, C., Wang, X., Zhang, Q., Wang, W., and Xue, L.: Ship emission of nitrous acid (HONO) and its impacts on the marine atmospheric oxidation chemistry, Sci. Total Environ., 735, 139355, https://doi.org/10.1016/j.scitotenv.2020.139355, 2020.
- Tan, W., Wang, H., Su, J., Sun, R., He, C., Lu, X., Lin, J., Xue, C., Wang, H., Liu, Y., Liu, L., Zhang, L., Wu, D., Mu, Y., and Fan, S.: Soil Emissions of Reactive Nitrogen Accelerate Summertime Surface Ozone Increases in the North China Plain, Environ. Sci. Technol., 57, 12782–12793, https://doi.org/10.1021/acs.est.3c01823, 2023.

- Wang, L., Chai, J., Gaubert, B., and Huang, Y.: A review of measurements and model simulations of atmospheric nitrous acid, Atmos. Environ., 347, 121094, https://doi.org/10.1016/j.atmosenv.2025.121094, 2025.
- Wang, T., Xue, L., Brimblecombe, P., Lam, Y. F., Li, L., and Zhang, L.: Ozone pollution in China: A review of concentrations, meteorological influences, chemical precursors, and effects, Sci. Total Environ., 575, 1582–1596, https://doi.org/10.1016/j.scitotenv.2016.10.081, 2017.
- Wang, X., Yi, W., Lv, Z., Deng, F., Zheng, S., Xu, H., Zhao, J., Liu, H., and He, K.: Ship emissions around China under gradually promoted control policies from 2016 to 2019, Atmos. Chem. Phys., 21, 13835–13853, https://doi.org/10.5194/acp-21-13835-2021, 2021.
- Wild, O., Zhu, X., and Prather, M. J.: Fast-J: Accurate Simulation of In- and Below-Cloud Photolysis in Tropospheric Chemical Models, J. Atmos. Chem., 37, 245–282, https://doi.org/10.1023/A:1006415919030, 2000.
- WRF-Chem Model Development Team: WRF-Chem (Weather Research and Forecasting model coupled with Chemistry) Model, GitHub [code], https://github.com/wrf-model/WRF, last access: 28 October 2025.
- Wu, D., Zhang, J., Wang, M., An, J., Wang, R., Haider, H., Xu-Ri, Huang, Y., Zhang, Q., Zhou, F., Tian, H., Zhang, X., Deng, L., Pan, Y., Chen, X., Yu, Y., Hu, C., Wang, R., Song, Y., Gao, Z., Wang, Y., Hou, L., and Liu, M.: Global and Regional Patterns of Soil Nitrous Acid Emissions and Their Acceleration of Rural Photochemical Reactions, J. Geophys. Res.-Atmos., 127, e2021JD036379, https://doi.org/10.1029/2021JD036379, 2022.
- Xue, C.: Substantially Growing Interest in the Chemistry of Nitrous Acid (HONO) in China: Current Achievements, Problems, and Future Directions, Environ. Sci. Technol., 56, 7375–7377, https://doi.org/10.1021/acs.est.2c02237, 2022.
- Xue, C., Ye, C., Kleffmann, J., Zhang, C., Catoire, V., Bao, F., Mellouki, A., Xue, L., Chen, J., Lu, K., Zhao, Y., Liu, H., Guo, Z., and Mu, Y.: Atmospheric measurements at Mt. Tai Part I: HONO formation and its role in the oxidizing capacity of the upper boundary layer, Atmos. Chem. Phys., 22, 3149–3167, https://doi.org/10.5194/acp-22-3149-2022, 2022.
- Xue, C., Chen, H., McGillen, M. R., Su, H., Cheng, Y., Kleffmann, J., Li, G., Cazaunau, M., Colomb, A., Sciare, J., DeWitt, L., Marchand, N., Sarda-Esteve, R., Petit, J.-E., and Kukui, A.: Role of Heterogeneous Reactions in the Atmospheric Oxidizing Capacity in Island Environments, Environ. Sci. Technol., 59, 3153–3164, https://doi.org/10.1021/acs.est.4c11647, 2025.
- Yang, X., Lu, K., Ma, X., Liu, Y., Wang, H., Hu, R., Li, X., Lou, S., Chen, S., Dong, H., Wang, F., Wang, Y., Zhang, G., Li, S., Yang, S., Yang, Y., Kuang, C., Tan, Z., Chen, X., Qiu, P., Zeng, L., Xie, P., and Zhang, Y.: Observations and modeling of OH and HO<sub>2</sub> radicals in Chengdu, China in summer 2019, Sci. Total Environ., 772, 144829, https://doi.org/10.1016/j.scitotenv.2020.144829, 2021.
- Ye, C., Zhou, X., Pu, D., Stutz, J., Festa, J., Spolaor, M., Tsai, C., Cantrell, C., Mauldin, R. L., Campos, T., Weinheimer, A., Hornbrook, R. S., Apel, E. C., Guenther, A., Kaser, L., Yuan, B., Karl, T., Haggerty, J., Hall, S., Ullmann, K., Smith, J. N., Ortega, J., and Knote, C.: Rapid cycling of reactive nitrogen in the marine boundary layer, Nature, 532, 489–491, https://doi.org/10.1038/nature17195, 2016.

- Ye, C., Zhang, N., Gao, H., and Zhou, X.: Photolysis of Particulate Nitrate as a Source of HONO and NO<sub>x</sub>, Environ. Sci. Technol., 51, 6849–6856, https://doi.org/10.1021/acs.est.7b00387, 2017.
- Ye, C., Lu, K., Ma, X., Qiu, W., Li, S., Yang, X., Xue, C., Zhai, T., Liu, Y., Li, X., Li, Y., Wang, H., Tan, Z., Chen, X., Dong, H., Zeng, L., Hu, M., and Zhang, Y.: HONO chemistry at a suburban site during the EXPLORE-YRD campaign in 2018: formation mechanisms and impacts on O<sub>3</sub> production, Atmos. Chem. Phys., 23, 15455–15472, https://doi.org/10.5194/acp-23-15455-2023, 2023.
- Zaveri, R. A., Easter, R. C., Fast, J. D., and Peters, L. K.: Model for Simulating Aerosol Interactions and Chemistry (MOSAIC), J. Geophys. Res., 113, D13204, https://doi.org/10.1029/2007JD008782, 2008.
- Zha, Q., Xue, L., Wang, T., Xu, Z., Yeung, C., Louie, P. K. K., and Luk, C. W. Y.: Large conversion rates of NO<sub>2</sub> to HNO<sub>2</sub> observed in air masses from the South China Sea: Evidence of strong production at sea surface?, Geophys. Res. Lett., 41, 7710–7715, https://doi.org/10.1002/2014GL061429, 2014.
- Zhang, H. (2025). Observation and simulation data of HONO in Coastal Regions of Fujian, China. Figshare [data set], https://doi.org/10.6084/m9.figshare.29827070.v2, 2025.
- Zhang, H., Zhou, X., Ren, C., Li, M., Liu, T., and Huang, X.: A systematic review of reactive nitrogen simulations with chemical transport models in China, Atmos. Res., 107586, https://doi.org/10.1016/j.atmosres.2024.107586, 2024a.
- Zhang, H., Ren, C., Zhou, X., Tang, K., Liu, Y., Liu, T., Wang, J., Chi, X., Li, M., Li, N., Huang, X., and Ding, A.: Improving HONO Simulations and Evaluating Its Impacts on Secondary Pollution in the Yangtze River Delta Region, China, J. Geophys. Res.-Atmos., 129, e2024JD041052, https://doi.org/10.1029/2024JD041052, 2024b.
- Zhang, J., Lian, C., Wang, W., Ge, M., Guo, Y., Ran, H., Zhang, Y., Zheng, F., Fan, X., Yan, C., Daellenbach, K. R., Liu, Y., Kulmala, M., and An, J.: Amplified role of potential HONO sources in O<sub>3</sub> formation in North China Plain during autumn haze aggravating processes, Atmos. Chem. Phys., 22, 3275–3302, https://doi.org/10.5194/acp-22-3275-2022, 2022a.
- Zhang, J., Ran, H., Guo, Y., Xue, C., Liu, X., Qu, Y., Sun, Y., Zhang, Q., Mu, Y., Chen, Y., Wang, J., and An, J.: High crop yield losses induced by potential HONO sources A modelling study in the North China Plain, Sci. Total Environ., 803, 149929, https://doi.org/10.1016/j.scitotenv.2021.149929, 2022b.
- Zhang, L., Wang, T., Zhang, Q., Zheng, J., Xu, Z., and Lv, M.: Potential sources of nitrous acid (HONO) and their impacts on ozone: A WRF-Chem study in a polluted subtropical region, J. Geophys. Res.-Atmos., 121, 3645–3662, https://doi.org/10.1002/2015JD024468, 2016.
- Zhang, L., Li, Q., Wang, T., Ahmadov, R., Zhang, Q., Li, M., and Lv, M.: Combined impacts of nitrous acid and nitryl chloride on lower-tropospheric ozone: new module development in WRF-Chem and application to China, Atmos. Chem. Phys., 17, 9733–9750, https://doi.org/10.5194/acp-17-9733-2017, 2017.
- Zhang, S., Sarwar, G., Xing, J., Chu, B., Xue, C., Sarav, A., Ding, D., Zheng, H., Mu, Y., Duan, F., Ma, T., and He, H.: Improving the representation of HONO chemistry in CMAQ and examining its impact on haze over China, Atmos. Chem. Phys., 21, 15809–15826, https://doi.org/10.5194/acp-21-15809-2021, 2021.

- Zhang, X., Tong, S., Jia, C., Zhang, W., Li, J., Wang, W., Sun, Y., Wang, X., Wang, L., Ji, D., Wang, L., Zhao, P., Tang, G., Xin, J., Li, A., and Ge, M.: The Levels and Sources of Nitrous Acid (HONO) in Winter of Beijing and Sanmenxia, J. Geophys. Res.-Atmos., 127, e2021JD036278, https://doi.org/10.1029/2021JD036278, 2022c.
- Zhang, X., Tong, S., Jia, C., Zhang, W., Wang, Z., Tang, G., Hu, B., Liu, Z., Wang, L., Zhao, P., Pan, Y., and Ge, M.: Elucidating HONO formation mechanism and its essential contribution to OH during haze events, Npj Clim. Atmos. Sci., 6, 55, https://doi.org/10.1038/s41612-023-00371-w, 2023.
- Zheng, B., Tong, D., Li, M., Liu, F., Hong, C., Geng, G., Li, H., Li, X., Peng, L., Qi, J., Yan, L., Zhang, Y., Zhao, H., Zheng, Y., He, K., and Zhang, Q.: Trends in China's anthropogenic emissions since 2010 as the consequence of clean air actions, Atmos. Chem. Phys., 18, 14095–14111, https://doi.org/10.5194/acp-18-14095-2018, 2018.
- Zhong, X., Shen, H., Zhao, M., Zhang, J., Sun, Y., Liu, Y., Zhang, Y., Shan, Y., Li, H., Mu, J., Yang, Y., Nie, Y., Tang, J., Dong, C., Wang, X., Zhu, Y., Guo, M., Wang, W., and Xue, L.: Nitrous acid budgets in the coastal atmosphere: potential daytime marine sources, Atmos. Chem. Phys., 23, 14761–14778, https://doi.org/10.5194/acp-23-14761-2023, 2023.